nature neuroscience

ARTICLES

https://doi.org/10.1038/s41593-018-0330-y

Dorsolateral septum somatostatin interneurons gate mobility to calibrate context-specific behavioral fear responses

Antoine Besnard[1,2,3,4], Yuan Gao[5,10], Michael TaeWoo Kim[1,2,3,4,10], Hannah Twarkowski[1,2,3,4], Alexander Keith Reed[1,2,3,4], Tomer Langberg[1,2,3,4], Wendy Feng[1,2,3,4], Xiangmin Xu[6], Dieter Saur[7,8], Larry S. Zweifel[9], Ian Davison[5] and Amar Sahay[1,2,3,4]*

Adaptive fear responses to external threats rely upon efficient relay of computations underlying contextual encoding to subcortical circuits. Brain-wide analysis of highly coactivated ensembles following contextual fear discrimination identified the dorsolateral septum (DLS) as a relay of the dentate gyrus–CA3 circuit. Retrograde monosynaptic tracing and electrophysiological whole-cell recordings demonstrated that DLS somatostatin-expressing interneurons (SST-INs) receive direct CA3 inputs. Longitudinal in vivo calcium imaging of DLS SST-INs in awake, behaving mice identified a stable population of footshock-responsive SST-INs during contextual conditioning whose activity tracked and predicted non-freezing epochs during subsequent recall in the training context but not in a similar, neutral context or open field. Optogenetic attenuation or stimulation of DLS SST-INs bidirectionally modulated conditioned fear responses and recruited proximal and distal subcortical targets. Together, these observations suggest a role for a potentially hard-wired DLS SST-IN subpopulation as arbiters of mobility that calibrate context-appropriate behavioral fear responses.

The execution of adaptive fear responses to environmental threats relies on efficient and faithful relay of computations underlying contextual encoding to subcortical and brainstem circuits. A considerable body of work emphasizes a role for hippocampal–cortical interactions in governing fear responses[1,2]. In contrast, a small number of studies have begun to edify the role of the DLS as a direct bridge between the hippocampus and subcortical and brainstem circuits[3,4] that subserve defensive behaviors[5]. The DLS is comprised of numerous subtypes of inhibitory interneurons[6,7] and receives direct monosynaptic inputs from hippocampal CA3, CA1 and subicular subfields[4]. Lesions studies support a role for the DLS in linking contextual information with action. Specifically, DLS lesions impair context-dependent cocaine reinstatement[8], whereas infusion of glutamic acid into DLS decreased context-dependent freezing behavior[9]. Pioneering single-unit recordings in lateral septum (LS) showed that aversive conditioned stimuli (CSs) decreased steady-state LS activity and appetitive conditioned stimuli increased LS activity[10], suggesting that the activity of LS cells may come under top-down control to regulate conditioned behavioral responses such as freezing or movement. Large-scale multisite recordings in hippocampus and LS revealed highly correlated spiking of LS neurons with hippocampal theta oscillations[11,12]. Because hippocampal theta oscillations are associated with learning and memory and contextual fear recall, these observations suggest that phase coding in lateral septum may permit integration of CA1 and CA3 inputs to transform hippocampal representations into context-appropriate behavioral responses[12].

The cellular heterogeneity of the DLS suggests potentially distinct roles for the different inhibitory interneuron cell types. Consistent with this notion, cell-type-specific targeting studies have begun to reveal roles of distinct lateral septum interneurons (LS-INs) in mediating effects of stress on fear and anxiety[13–15] or on social behavior[16]. In contrast, we know less about the identities of inhibitory interneurons within the DLS that relay context-dependent information to calibrate conditioned responses. Addressing this gap in our knowledge necessitates identifying which DLS-IN populations are physiologically recruited by conditioned stimuli and causative assessment of functional contributions of DLS-INs to calibration of fear responses.

Here we undertook an agnostic brain-wide analysis of coactivated ensembles under conditions of high and low contextual fear discrimination, and we identified a noncanonical dentate gyrus (DG)–CA3–DLS circuit whose activity was most highly correlated to discrimination performance. Within the DLS, we found that SST-INs are broadly distributed and receive monosynaptic inputs from CA3 as assessed by retrograde monosynaptic tracing and electrophysiological whole-cell recordings. Longitudinal in vivo calcium imaging of DLS SST-INs in awake, behaving mice identified a stable population of footshock responsive SST-INs (SST^{FSH} cells) during contextual fear conditioning whose activity tracked non-freezing epochs during subsequent recall in the training context but not in

---

[1]Center for Regenerative Medicine, Massachusetts General Hospital, Boston, MA, USA. [2]Harvard Stem Cell Institute, Cambridge, MA, USA. [3]Department of Psychiatry, Massachusetts General Hospital, Harvard Medical School, Boston, MA, USA. [4]BROAD Institute of Harvard and MIT, Cambridge, MA, USA. [5]Department of Biology, Boston University, Boston, MA, USA. [6]Departments of Anatomy and Neurobiology and Biomedical Engineering, School of Medicine, University of California, Irvine, CA, USA. [7]Division of Translational Cancer Research, German Cancer Research Center (DKFZ) and German Cancer Consortium (DKTK), Im Neuenheimer Feld 280, Heidelberg, Germany. [8]Institute of Translational Cancer Research and Experimental Cancer Therapy, and Department of Medicine II, Technische Universität Munchen, Munich, Germany. [9]Department of Psychiatry and Behavioral Science, University of Washington, Seattle, WA, USA. [10]These authors contributed equally: Yuan Gao, Michael TaeWoo Kim. *e-mail: asahay@mgh.harvard.edu

a similar, neutral context or open field. Furthermore, SST^{FSH} cell activity during freezing and non-freezing transitions was sufficient to train a decoder to reliably predict freezing epochs. Optogenetic attenuation or stimulation of DLS SST-INs bidirectionally modulated context-dependent conditioned fear responses and recruited diverse proximal and distal subcortical targets. Together, these observations uncover previously underappreciated functional heterogeneity in DLS SST-INs and suggest a role for a stable, potentially hardwired population of DLS SST-INs as sensors of conditioned threat and arbiters of mobility that calibrate context appropriate behavioral fear responses.

Results

Contextual fear discrimination is associated with activation of DG–CA3–DLS circuit. To identify brain networks that underlie discrimination of contextual threats, we systematically mapped neuronal activation in mice that were efficient or poor discriminators using c-Fos immunohistochemistry. We trained two cohorts of C57BL/6J mice in a contextual fear-conditioning discrimination learning paradigm (CFCDL) in which mice were challenged to discriminate between a context associated with a footshock (Fig. 1a) and a distinct or similar neutral context (Fig. 1a,b)[17,18]. As expected based on context similarity, mice exposed to the conditioning context A and similar context A′ (AA′) exhibited poor discrimination (high levels of freezing in context A′), whereas the cohort of mice exposed to the conditioning context A and distinct context B (AB) exhibited high levels of discrimination (low levels of freezing in context B) (Fig. 1b–d). Brain-wide analysis of the immediate early gene c-Fos protein in AB and AA′ cohorts of mice 60 min after exposure to the neutral similar or distinct context (Fig. 1e) permitted identification of brain regions with three different patterns of c-Fos immunoreactivity: (i) brain regions whose levels of c-Fos immunoreactivity were unchanged compared with naïve controls (Fig. 1f and Supplementary Figs. 1 and 2a); (ii) brain regions whose levels of c-Fos immunoreactivity were sensitive to context exposure but unrelated to discrimination efficiency (Fig. 1f and Supplementary Fig. 1 and 2a); and (iii) brain regions whose levels of c-Fos immunoreactivity were highly sensitive to discrimination performance (Fig. 1f and Supplementary Figs. 1 and 2a). Increased discrimination efficiency (lower freezing levels in neutral context B) was associated with higher c-Fos immunoreactivity in CA3, caudate putamen (CPUm), lateral region of anterior DLS (aDLS) (Supplementary Fig. 3), diagonal band nucleus (DBN), nucleus accumbens (NAcc), dorsomedial periaqueductal gray (PAGdm) and lateral supramammillary nucleus (SUMl) and lower c-Fos levels in the lateral amygdala (LA), ventral bed nucleus of stria terminalis (vBNST), posterior paraventricular thalamus (PVT) and paraventricular nucleus of hypothalamus (PVN)(Fig. 1f and Supplementary Figs. 1 and 2a). Because c-Fos immunoreactivity occurs rapidly and transiently in DG upon contextual fear retrieval[19], we repeated this experiment for c-Fos analysis in AB and AA′ cohorts of mice 30 min after exposure to the neutral similar or distinct context. This experiment revealed a higher number of c-Fos immunoreactive cells in the DG of mice exhibiting lower levels of freezing in context B relative to context A′ (Supplementary Figs. 1a and 2c–e).

We then sought to identify putative brain networks underlying contextual fear discrimination by generating a correlation matrix from the c-Fos data using a within- and between-subject design[20] (Fig. 1g and Supplementary Fig. 2a). Our unbiased analyses identified correlations with varying strength (Fig. 1g, statistical strength) and directionality (Fig. 1g, Spearman *r*) between different brain regions. Correction for multiple comparisons identified a putative CA3–DLS network whose activity was most highly correlated with discrimination efficiency (low levels of freezing in neutral context B) (Fig. 1h and Supplementary Fig. 2b).

To rule out the possibility that c-Fos levels reflected increased exploratory behavior rather than contextual fear discrimination, we trained four new groups of C57BL/6J mice in the same contextual fear discrimination learning task (Supplementary Fig. 2f), but only two groups were shocked in context A throughout the 10-day conditioning protocol and were re-exposed either to context A or to context B on day 11. The other two groups of mice underwent the same conditioning protocol without receiving any footshock and were re-exposed either to context A or to context B on day 11 (Supplementary Fig. 2f). On day 11, as expected, only the footshock-conditioned mice exposed to context A displayed significant elevation in freezing behavior in context A (Supplementary Fig. 2g). Importantly, the animals exposed to context B after conditioning to context A showed significantly higher levels of c-Fos in the anterior DLS compared with the other groups (Supplementary Fig. 2h–j). Together, these observations suggest that contextual fear discrimination, but not context exposure, preferentially activates a CA3–DLS circuit. Because CA3 neurons project to the DLS[3,8,11,12,21] (Supplementary Fig. 4d), this pathway may broadcast hippocampal computations to subcortical brain regions to calibrate context-appropriate fear responses.

DLS SST-INs receive direct monosynaptic CA3 inputs. The DLS is made up of only inhibitory neurons and not excitatory neurons. As a first step toward mapping DLS afferents, we injected a canine-associated virus-2 encoding Cre recombinase into DLS of Ai14 reporter mice (Supplementary Fig. 4). Consistent with a previous study in the rat[4], we found that the DLS receives monosynaptic inputs from several different brain regions, including the subiculum, medial septum and diagonal band nuclei, hippocampal CA3 and CA2, prefrontal cortex, and thalamic and hypothalamic nuclei (Supplementary Fig. 4a–c).

Immunohistochemical analyses of different markers of inhibitory interneuron subtypes delineated unique distribution patterns along the mediolateral axis of the DLS and revealed that SST-INs were the most abundant DLS-INs[22] (Supplementary Fig. 5a; http://mouse.brain-map.org/experiment/show/1001). Immunohistochemical analysis and examination of mice in which inhibitory interneurons (Gad2-Cre::Ai14) or SST-INs (SST-Cre::Ai14) were genetically labeled with tdTomato suggested that SST-INs comprise a large proportion of GABAergic DLS-INs along the anteroposterior axis of the DLS (Supplementary Fig. 5b–e). Analysis of termination fields of DLS SST-INs revealed long-range projections to the lateral hypothalamus, bed nucleus of stria terminalis and supramammillary nucleus that were largely overlapping with projections of Gad2-expressing DLS-INs (Supplementary Fig. 5f). Based on these characteristics, we sought to address whether DLS SST-INs receive direct hippocampal inputs.

In order to identify presynaptic partners of SST-INs, we performed pseudotyped rabies virus trans-synaptic retrograde tracing[23,24]. Infection with modified rabies virus (Env-A pseudotyped RABV lacking G glycoprotein and expressing mCherry, SADΔG-mCherry) is restricted to a specific, labeled population of starter cells expressing the avian receptor TVA, and limits tracing to first-order presynaptic partners, as further trans-synaptic spread is abrogated in the absence of glycoprotein. We bred SST-Cre mice with a conditional TVA-expressing mouse line (LSL-TVA) to generate SST-Cre::TVA mice[25] (Fig. 2a). We injected conditional AAV helper virus expressing GFP and EnvA pseudotyped G-deleted rabies virus in DLS of SST-Cre::TVA mice, identified starter cells (GFP$^+$mCherry$^+$) in the DLS (Fig. 2a) and mapped the presynaptic cells (mCherry$^+$) in the medial septum (MS), DBN, dSubiculum, CA1 and CA3 (Fig. 2b). Within the hippocampus, we found that CA3, CA1 and dSubiculum form monosynaptic contacts with DLS SST-INs. DLS SST-INs also received direct inputs from other DLS cells as well as PFCx, LH and SUM, albeit to a lower extent (Fig. 2b).

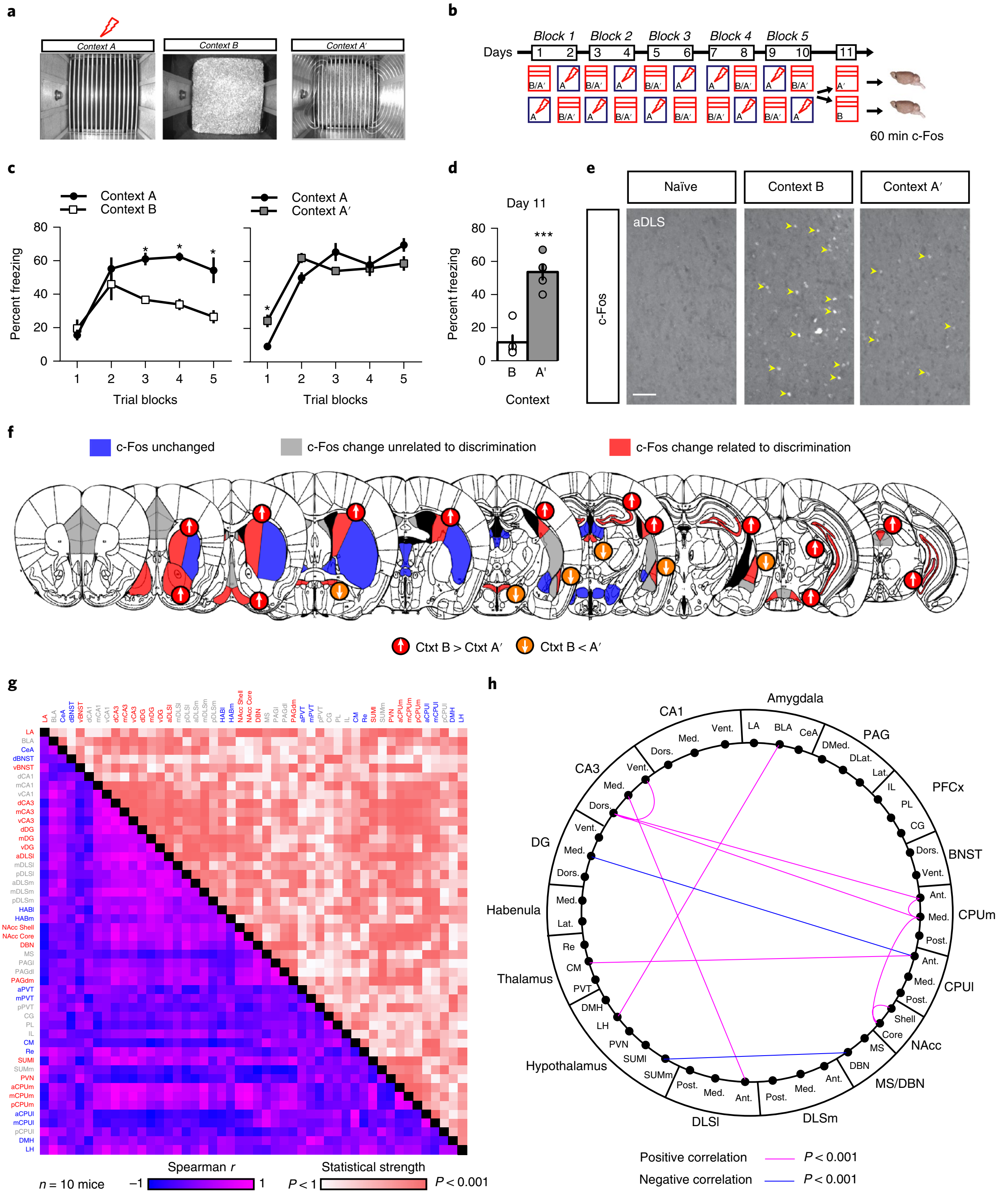

Fig. 1 | Contextual fear discrimination is associated with activation of a DG–CA3–DLS network. a,b, Schematic representation of CFCDL procedure in which mice were trained to discriminate between a footshock delivered in context A and a safe context B (group AB) or A′ (group AA′). **c**, Freezing behavior in AB and AA′ groups over five blocks of training. Means ± s.e.m.; $n = 5$, 5 mice per group, mixed-factor two-way ANOVA (repeated measures over time); group AB: time $F_{(4,32)} = 13.83$, $P < 0.001$; context $F_{(1,8)} = 20.83$, $P < 0.01$; interaction $F_{(4,32)} = 3.676$, $P < 0.01$; group AA′: time $F_{(4,32)} = 47.71$, $P < 0.001$; context $F_{(1,8)} = 0.04855$, not significant; interaction $F_{(4,32)} = 5.043$, $P < 0.01$. $^{*}P < 0.05$, context A versus context B or A′. **d**, Freezing behavior during final exposure to the safe context. Means ± s.e.m.; $n = 5$, 5 mice per group, unpaired Student's two-tailed t test, $^{***}P < 0.001$, context B versus A′. **e**, c-Fos immunohistochemistry (yellow arrowheads) in mice previously exposed to context (ctxt) B or A′, as well as a naïve control group. Representative images for five independent animals per group. Scale bar, 50 μm. **f**, Schematic depicting brain-wide c-Fos analysis in AB and AA′ mice compared with naïve controls. c-Fos immunoreactivity unchanged (blue), B and A′ different from naïve (gray), and B and A′ different from each other (red). Arrows indicate c-Fos changes in relation to freezing behavior. **g,** Inter-regional correlations for brain-wide c-Fos immunoreactivity using within- and between-subject design in context A′ and B. **h**, Schematic representation of the most robust inter-regional correlations (data are corrected for multiple comparisons). Note the robust positive correlations between CA3 and DLS but not CA1. See methods and statistics detailed in Supplementary Tables 1 and 2.

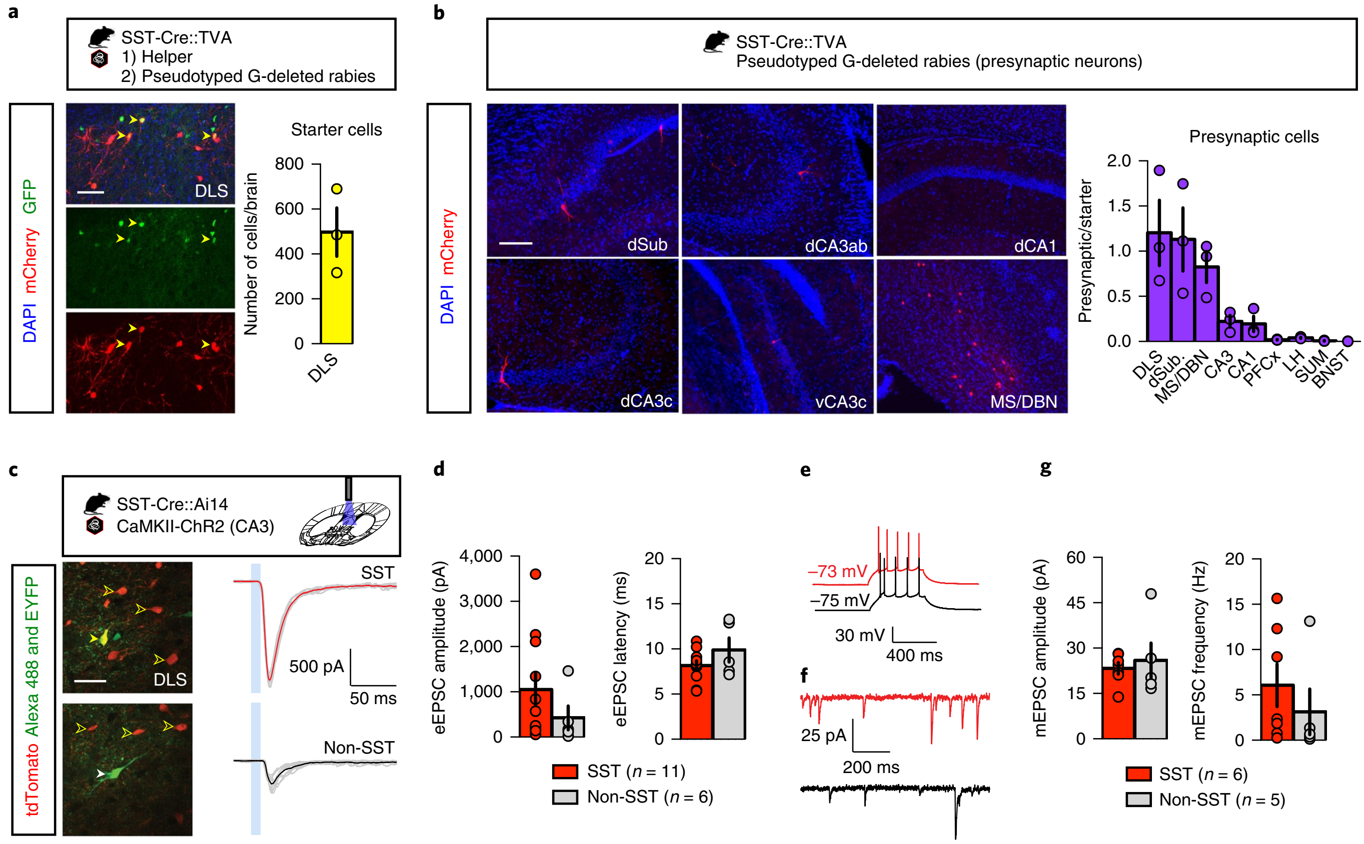

Fig. 2 | DLS SST-INs receive direct monosynaptic inputs from CA3. a, SST-Cre::TVA bigenic mice were injected with helper virus (AAV8-EF1a-FLEX-HB) followed by pseudotyped G-deleted rabies virus (EnvA-SADΔG-mCherry) in the DLS. Yellow arrowheads denote starter cells, which are positive for both GFP (helper) and mCherry (rabies). Representative images for three independent animals. Scale bar, 50 µm. Means ± s.e.m.; *n* = 3 mice per group. **b**, Presynaptic partners were identified in the MS/DBN, dorsal subiculum, CA1, dorsal and ventral CA3. Representative images for three independent animals. Scale bar, 100 µm. Means ± s.e.m.; *n* = 3 mice per group. **c**, Example recordings of blue-light-evoked monosynaptic inputs onto DLS neurons in acute slices obtained from adult SST-Cre::Ai14 bigenic mice. Yellow outlined arrowheads indicate tdTomato-labeled SST-INs; solid yellow arrowhead indicate dye fills of the recorded cell. Representative images for four independent animals. Scale bar, 30 µm. Traces show synaptic currents evoked in both SST-INs (top) and non-SST INs (bottom), and the 10 ms light pulse is indicated by a blue box. Individual trials are shown in gray, and averages are shown in red and black. **d**, Average amplitude and latency for both cell types. Means ± s.e.m; *n* = 11, 6 cells per group, unpaired Student's two-tailed *t* test. **e,** Firing properties of SST- and non-SST-INs tested by current injection. **f**, Example recordings of miniature synaptic currents in SST neurons (red) and non-SST cells (black). **g**, Amplitude and frequency for mEPSCs in SST- and non-SST-INs. Means ± s.e.m.; *n* = 6, 5 cells per group, Student's two-tailed *t* test. All statistics are detailed in Supplementary Table 1.

We characterized the functional connections from CA3 onto SST-INs by optogenetic stimulation of CA3–DLS projections in ex vivo brain slices. To this end, we recorded from tdTomato-labeled DLS SST-INs and non-labeled DLS cells after blue light stimulation of CA3 terminals expressing ChR2 in DLS of SST-Cre::Ai14 mice (Fig. 2c). Recordings were performed in the presence of TTX (1 µM) and 4-AP (100 µM) to ensure that responses reflected monosynaptic connections. Both labeled and non-labeled DLS populations consistently received synaptic input from CA3 (synaptic responses detected in 11/11 SST and 5/6 non-SST neurons). Although the size of responses was variable in both populations, inputs to DLS SST-INs were particularly strong, often exceeding 2,000 pA (Fig. 2d). Inputs to non-SST neurons, while still robust, were typically smaller (Fig. 2d, six neurons each in 4 mice). Firing properties of SST- and non-SST-INs tested by current injection were indistinguishable (Fig. 2e). To estimate the size of single-synapse inputs, we also recorded miniature excitatory postsynaptic currents (mEPSCs) in a subset of cells (Fig. 2f). Mean mEPSC amplitudes were 22 and 24 pA for DLS SST-INs and non-SST INs, respectively, suggesting that ChR2-mediated responses comprised a large number of individual synaptic contacts (Fig. 2g). Together, these data indicate that DLS SST-INs receive direct robust functional inputs from CA3 and are positioned to relay contextual information to gate action.

A stable DLS SST-IN subpopulation recruited during contextual fear conditioning predicts mobility states during recall in the conditioned context. Central to understanding the contributions of DLS SST-INs to behavior is a characterization of physiological activation patterns of DLS SST-INs in awake, behaving mice over time and across behavioral tasks. To this end, we performed live calcium imaging[26] using miniature endoscopes (500 µm wide GRIN lens) after selective expression of the genetically encoded calcium indicator GCaMP6m[27] in DLS SST-INs by injecting AAV-DJ-DIO-GCaMP6m into DLS of SST-Cre mice (Fig. 3a, SST-Cre::Ai14). GCaMP6m expression was confirmed via assessment of cytoplasmic GCaMP6m, and nuclear c-Fos expression was observed in SST cells of bigenic SST-Cre::Ai14 mice after testing (Supplementary Fig. 6a). Installation of a baseplate permanently above the GRIN lens permitted longitudinal imaging in vivo of 121 cells in eight animals (Fig. 3b; Supplementary Figs. 7 and 8) across ten recording sessions (3 min/session) including open-field (OF), elevated plus maze (EPM), contextual fear conditioning (CFC1 and CFC2, 3 footshocks/session) in training context A and recall sessions in context A or a distinct, neutral context B (Fig. 3c). After motion correction, cells were segmented using the automated algorithm, constrained non-negative matrix factorization optimized for micro-Endoscopic data (CNMF-E). Calcium transients were detected in each of the 121 recorded cells, and average calcium transient frequencies (Hz) were calculated for each recording session (Fig. 3d, Supplementary Fig. 6b and Supplementary Videos 1 and 2).

We first evaluated population-level SST-IN calcium dynamics in the OF and EPM (Fig. 3e,f). Over two consecutive days, SST-INs exhibited lower calcium (Ca^{2+}) transient frequencies in the center of the OF compared with the periphery and corners (Fig. 3e,f and Supplementary Fig. 6c). Consistent with single unit recordings in the LS[28], Ca^{2+} transient frequency in SST-INs was greater in the open arms of the EPM compared with the center or closed arms (Fig. 3e–g; Supplementary Fig. 6d). After the first session of contextual fear conditioning (3×2 s at 0.7 mA footshock/session), mice displayed high levels of freezing behavior in context A but not context B (Fig. 3d). Freezing responses were comparable across multiple sessions over 2 days, thus suggesting negligible extinction of the conditioned response (Supplementary Fig. 6e–g). We found that SST-INs Ca^{2+} frequency was significantly higher during non-freezing epochs versus freezing epochs in both context A and context B (Fig. 3g,h). Furthermore, we found that SST-INs Ca^{2+} frequency was significantly higher during non-freezing epochs in context A versus context B (Fig. 3h). Similarly, we observed an elevation in Ca^{2+} transient amplitude during non-freezing epochs relative to freezing epochs in context A (Supplementary Fig. 6l). Comparison of SST-IN Ca^{2+} transient frequency during mobility and immobility epochs in the OF versus freezing and non-freezing epochs in context A revealed that SST-INs are generally more active during periods of mobility/non-freezing epochs across these tests (Fig. 3h).

These observations motivated us to ask whether SST-INs may be heterogeneous and whether a stable (rather than a stochastically allocated) population is recruited to govern mobility in the conditioned context. Towards this goal, we sorted all 121 cells based on calcium transients evoked by footshocks during CFC1 and CFC2 (Fig. 3i) and identified 22 cells (18% of total population) that responded to footshocks during CFC1 and CFC2 sessions (SST^{FSH}). Comparison of activity of SST^{FSH} cells with that of a null distribution at the onset of the footshocks suggested that SST^{FSH} cells were not stochastically recruited (see Methods) (one-sample *z* test, $P<0.05$). Additionally, we found that 64 cells (52% of total population) did not respond to footshocks in CFC1 or CFC2 ($SST^{non\text{-}FSH}$) and a smaller number of cells that responded to footshock either in CFC1 or in CFC2 (16 cells CFC1, 19 cells CFC2 (Fig. 3i). We then compared our experimental data (real overlap across CFC1 and CFC2), against null distributions for SST^{FSH} and $SST^{non\text{-}FSH}$ (Fig. 3j,k). Our analysis revealed a significant difference between the real overlap and the null distribution for both SST^{FSH} and $SST^{non\text{-}FSH}$ cells (Fig. 3j,k) suggesting that these cell populations reflect discrete and stable DLS SST-IN populations. Importantly, principal component analysis and independent component analysis (PCA-ICA) analyses yielded the same conclusions even though the absolute numbers of SST^{FSH} and $SST^{non\text{-}FSH}$ cells were different (Supplementary Fig. 6h–k).

We then asked whether the activity of stable SST^{FSH} cell subpopulation tracks and permits decoding of behavior. Activity of SST^{FSH} cells was significantly higher during non-freezing epochs than $SST^{non\text{-}FSH}$ in context A (Fig. 3l) and, unlike $SST^{non\text{-}FSH}$ cell activity or shuffled cell activity, was finely tuned to freezing–non-freezing transitions in the conditioned context (context A) (Fig. 3m). Specifically, activity of SST^{FSH} cells decreased during onset of freezing epoch and increased as mice stopped freezing (Fig. 3m). Next, we performed a decoder analysis across mice ($n=6$ mice for SST^{FSH} cells, $n=8$ mice for $SST^{non\text{-}FSH}$ cells) using the local maxima and local minima of the instantaneous rates of change (for freezing offset and onset, respectively) for SST^{FSH} and $SST^{non\text{-}FSH}$ cells (Fig. 3n,o). The decoder based on SST^{FSH} cell activity, but much less so on $SST^{non\text{-}FSH}$ cell activity, robustly and faithfully predicted freezing epochs in the conditioned context A but not in the neutral context B or in the OF (immobility onset or offset)(Fig. 3n,o and Supplementary Fig. 6q).

To determine whether a stable subpopulation of SST-INs was recruited in anxiety tests, we examined SST-INs that were active during mobility epochs in the OF (OF1 and OF2; Supplementary Fig. 6m) and during exploration of EPM (EPM1 and EPM2; Supplementary Fig. 6o). In contrast to what we found with SST^{FSH} and $SST^{non\text{-}FSH}$ cells, the real overlap between cells recruited during mobility (SST^{MOB}) epochs in OF1 and OF2 (39/121 cells) or exploration of the open arms (SST^{OA}) during EPM1 and EPM2 (5/121) cells was not different from the null distribution, suggestive of stochastic recruitment of these cell populations during these anxiety tests (Supplementary Fig. 6n,p).

Together, these results suggest that DLS SST-INs are functionally heterogeneous and identify a potentially hard-wired population of SST^{FSH} cells that are physiologically recruited during behavioral state transitions in the conditioned context.

Optogenetic silencing of DLS SST-INs increases contextual fear responses. To determine the functional contribution of DLS SST-INs to innate anxiety and contextual fear discrimination, we used optogenetics to attenuate the activity of SST-INs cell bodies in DLS. We bilaterally injected rAAV5-DIO-eNpHR3.0 (double-*loxP*-flanked inverted orientation; halorhodopsin) or rAAV5-DIO-EYFP (enhanced yellow fluorescent protein) control viruses into DLS of SST-Cre mice (Supplementary Fig. 9a), implanted fiber optics above the DLS (Supplementary Fig. 9b) and proceeded with behavioral testing as schematized (Fig. 4a–c). Green-light-induced silencing of SST-INs in DLS did not alter locomotion and behavioral measures of innate anxiety in OF, EPM and novelty suppressed feeding (NSF) (Fig. 4d–g). In the extended version of CFCDL (contextual fear conditioning discrimination learning) paradigm, both DIO-EYFP and DIO-eNpHR3.0 groups learned to discriminate between contexts A and B (Fig. 4h). Silencing SST-INs increased freezing levels in both contexts A and B (Fig. 4h, block 7) without changing discrimination specificity (Fig. 4i). The overall increase in freezing behavior observed in response to SST-INs silencing was primarily driven by an increase in the number of freezing bouts and to lesser extent by increased freezing-bout duration (Supplementary Fig. 9d–g). We found that optogenetic silencing of SST-INs resulted in decreased activation of vBNST, CPUm, PVN, BLA, vCA3, vCA1 and PAGl, as quantified by c-Fos immunoreactivity 60 min post exposure to context B (Fig. 4j,k). Together, these findings demonstrate that DLS SST-INs normally constrain conditioned fear responses (such as freezing in training context) by supporting mobility and that these effects are potentially mediated via their projections to diverse subcortical brain areas.

Optogenetic stimulation of DLS SST-INs attenuates anxiety and contextual fear responses. We next used optogenetics to activate cell bodies of SST-INs in DLS. We bilaterally injected rAAV5-DIO-ChR2 (double-*loxP*-flanked inverted orientation; channelrhodopsin-2) or rAAV5-DIO-EYFP (enhanced yellow fluorescent protein) control viruses into DLS of SST-Cre mice, implanted fiber optics above the DLS (Supplementary Fig. 9c) and proceeded with behavioral testing as schematized (Fig. 5a–c). Blue light stimulation (15 Hz) of SST-INs in DLS reversibly increased the time spent in the open arms in the EPM (Fig. 5f) without altering horizontal activity and behavioral measures of innate anxiety in OF and novelty suppressed feeding (NSF)(Fig. 5d,e,g). In the extended version of the CFCDL (contextual fear conditioning discrimination learning) paradigm, both DIO-EYFP and DIO-ChR2 groups learned to discriminate between contexts A and B (Fig. 5h, blocks 1–6). Stimulating

SST-INs activity decreased freezing levels in contexts A and B (Fig. 5h, block 7) without changing discrimination specificity (Fig. 5i). The overall decrease in freezing behavior observed in response to SST-INs stimulation was primarily driven by a decrease in freezing bout duration (Supplementary Fig. 9h–k). We found that optogenetic stimulation of SST-INs (Supplementary Fig. 9l–n) resulted in increased activation of DLS, BNST, CPUm, posterior CPUl and lateral SUM as quantified by c-Fos immunoreactivity 60 min post exposure to context B (Fig. 5j,k). Together, these findings demonstrate that 15 Hz stimulation of DLS SST-INs is sufficient to decrease conditioned fear responses and anxiety potentially via their projections to diverse subcortical brain areas.

Discussion

Adaptive defensive behavior necessitates faithful and expeditious relay of computations underlying discrimination of threats to subcortical and brainstem circuits governing fight and flight responses. The DG–CA3 circuit is thought to mediate encoding and discrimination of contextual information[17,21,29–34]. Our brain-wide analysis of coactivated ensembles under conditions of high and low contextual fear discrimination conditions identified a CA3–DLS, rather than the CA3–CA1, circuit as highly sensitive to contextual fear discrimination. While the specific contribution of CA3–DLS excitatory projections to contextual discrimination remains to be fully elucidated, we recently reported that dorsal excitatory CA2/CA3 projections to DLS control the discrimination of social stimuli[35]. Thus, the CA2/CA3–DLS pathway may permit rapid linkage of computations in DG–CA3 underlying the discrimination of social or contextual cues with subcortical circuits without undergoing modifications in the canonical CA3/CA2–CA1–subiculum pathway[36,37].

The DLS is made up of inhibitory interneurons whose physiological and functional contributions to defensive responses remain poorly understood[5,6]. Longitudinal in vivo calcium imaging permitted assessment of physiological recruitment of DLS SST-INs in anxiety tasks and contextual fear conditioning and recall. Because of our ability to image SST-INs over time and across tasks in the same animals, we discovered a discrete, non-stochastically allocated subpopulation of SST-INs that were consistently recruited by footshocks during CFC (≈18% of total population). Importantly, the activity of $\mathrm{SST^{FSH}}$ cells was finely tuned to non-freezing epochs in the conditioned but not a neutral, safe context. Furthermore, $\mathrm{SST^{FSH}}$ cell activity was specifically linked to defensive responses (freezing behavior) and not general, immobile-to-mobile state transitions in the open field. Decoding the activity of $\mathrm{SST^{FSH}}$ cells faithfully and reliably predicted freezing behavior in the conditioned context, but not in neutral, safe context and did not predict immobility epochs in the open field. The $\mathrm{SST^{FSH}}$ subpopulation may represent the population of cells captured in single-unit recordings in the lateral septum whose activity inversely tracked aversive conditioned stimuli[10]. Our findings, together with those of a recent study that implicated a DLS SST-IN population in regulation of feeding behavior[38], suggest that SST-INs, much like in the cortex, are heterogeneous and that the $\mathrm{SST^{FSH}}$ cells serve as arbiters of mobility in the conditioned context.

Hardwired differences in afferent inputs and state-dependent recruitment of inputs onto SST-INs may dictate behavior-specific activation patterns of distinct subpopulations[39,40]. Our pseudotyped rabies-based tracing studies and ex vivo slice physiology cannot distinguish difference in input–output relationships at the level of single SST-INs. It is plausible that DLS SST-INs may differ in the extent to which they receive monosynaptic inputs from diverse higher cortical regions (CA3, dSub, CA1, PFCx) and subcortical regions (MS/DBN, LH and SUM) and other intermingled DLS-INs. For instance, a recent study identified discrete cholinergic subpopulations in the basal forebrain based on different patterns of monosynaptic inputs and outputs[41]. The identification of molecular signatures underlying heterogeneity of DLS SST-INs as previously done for neocortical SST-INs[42] in combination with in vivo imaging and input–output mapping approaches will edify the basis of non-stochastic allocation of DLS SST-INs in contextual fear processing.

Consistent with the physiological patterns of SST-INs activity identified using longitudinal calcium imaging, optogenetic silencing and stimulation of DLS SST-INs bidirectionally increased or decreased fear responses (freezing levels) in both the conditioned context and a similar, safe context. Analysis of brain regions

Fig. 3 | A stable subpopulation of SST-INs is recruited during fear conditioning and predicts freezing behavior during recall. a, GFP immunohistochemistry (GCaMP6m) and tdTomato expression in SST-Cre::Ai14 bigenic mice. Nuclei are counterstained with DAPI. Scale bar, 200 µm. Red horizontal bar indicates field of view. **b**, Field of view for in vivo GCaMP6m signal restricted to SST-INs in DLS. Representative image for 8 independent animals. Yellow arrowheads indicate representative cells with observable variations of fluorescence across time (maximum projection). Scale bar, 100 µm. **c**, Timeline of longitudinal calcium imaging experiments. **d**, Example of calcium transients detected with CNMF-E from 7 different cells during exposure to context A and context B during freezing (gray bars) and non-freezing epochs (representative of 8 independent animals). Note the limited number of transients during freezing epochs. Scale bar: *x* axis,10 s; *y* axis: 5 s.d. **e**, Heat maps indicate the percent time (% total) spent in the different zones of the OF and EPM on two consecutive sessions. **f**, Heat maps indicate the calcium transient frequency (Hz) for 121 cells detected with CNMF-E per zone in the OF and EPM on two consecutive sessions. **g**, Raster plot of calcium transient frequency (Hz) detected with CNMF-E (average of session 1 and 2) in OF and EPM during freezing and non-freezing epochs in context A and B. Sorting of 121 cells based on their responsiveness to the first 3 footshocks administered during CFC1 (black arrow). **h**, Average calcium transient frequency (Hz) for the overall population ($n = 121$ cells) identified with CNMF-E in the OF, EPM, context A and context B (average of two consecutive sessions). Means ± s.e.m. and data distribution represented as violin plots; $n = 121$ cells, one-way analysis of variance (ANOVA) (repeated measures over time) followed by Tukey's multiple comparisons post hoc test. $^*P < 0.05$. **i**, Sorting of the 121 cells detected with CNMF-E based on calcium transients observed in response to footshocks delivered during CFC1 and CFC2. Cells that never responded to footshocks, gray; cells that responded to 1, 2 or 3 footshocks during CFC1, blue, and CFC2, green. Cells that responded to footshocks during both CFC1 and CFC2, red. **j**,**k**, Probability density function (PDF) for overlap between $\mathrm{SST^{FSH}}$ cells (22/121) and $\mathrm{SST^{non\text{-}FSH}}$ cells (64/121) detected with CNMF-E across CFC1 and CFC2 with a truncated null distribution. **l**, Average calcium transient frequency (Hz) for $\mathrm{SST^{FSH}}$ cells and $\mathrm{SST^{non\text{-}FSH}}$ cells during freezing (red) and no freezing (blue) events in context A and context B. Means ± SEM and data distribution represented as violin plots; $n = 22,64$ cells, one-way ANOVA followed by Tukey's multiple comparisons post hoc test across no freezing events, $^*P < 0.05$, $\mathrm{FSH^+}$ cells in context A versus all groups. **m**, Calcium transient frequency analysis for behavioral state transitions for $\mathrm{SST^{FSH}}$ cells, $\mathrm{SST^{non\text{-}FSH}}$ cells or a randomly assigned cell population of equivalent size to that of $\mathrm{SST^{FSH}}$ cells. Behavioral state transitions consist in the onset (off–on) and offset (on–off) of freezing bouts (gray area) in context A or context B as well as immobility bouts in the open field (gray area). Means ± s.e.m.; $n = 22, 64, 100$ cells per group, mixed factor two-way ANOVA (repeated measure over time) followed by Bonferroni's multiple comparisons post hoc test across contexts, $^*P < 0.05$, $\mathrm{Ca^{2+}}$ frequency in context A versus all groups. **n**,**o**, Decoder analysis across mice based on calcium transient frequency local minima (**n**) and local maxima (**o**) predicting behavioral state transitions (freezing or immobility) in context A (blue), context B (red) or OF (green) using 1, 2 or 3 $\mathrm{SST^{FSH}}$ cells or $\mathrm{SST^{non\text{-}FSH}}$ cells per mouse. Means ± s.e.m.; $n = 6,8$ mice per group, mixed factor two-way ANOVA (repeated measure over time) and one sample Student's two-tailed *t* test, $^*P < 0.05$, data point versus chance. All statistics are detailed in Supplementary Table 1.

innervated by DLS SST-INs in conjunction with optogenetic-induced inhibition and activation patterns suggests roles for other DLS-INs and diverse subcortical targets (BNST, CPUm, posterior CPUl, PAGl, BLA, lateral SUM) in mediating freezing levels. How and whether these targets regulate physiological changes such as heart rate or blood pressure remains to be determined[5]. Interestingly, the vBNST and CPUm exhibited bidirectional changes in c-Fos expression following optogenetic stimulation and inhibition of SST-INs raising the intriguing possibility that they may be under control of two distinct SST-IN subpopulations.

How is the SST^{FSH} cell dependent gating of mobility in the conditioned context achieved at a circuit level? Recent findings suggest that phase coding in DLS may represent a circuit-based mechanism by which hippocampal representations supported by theta

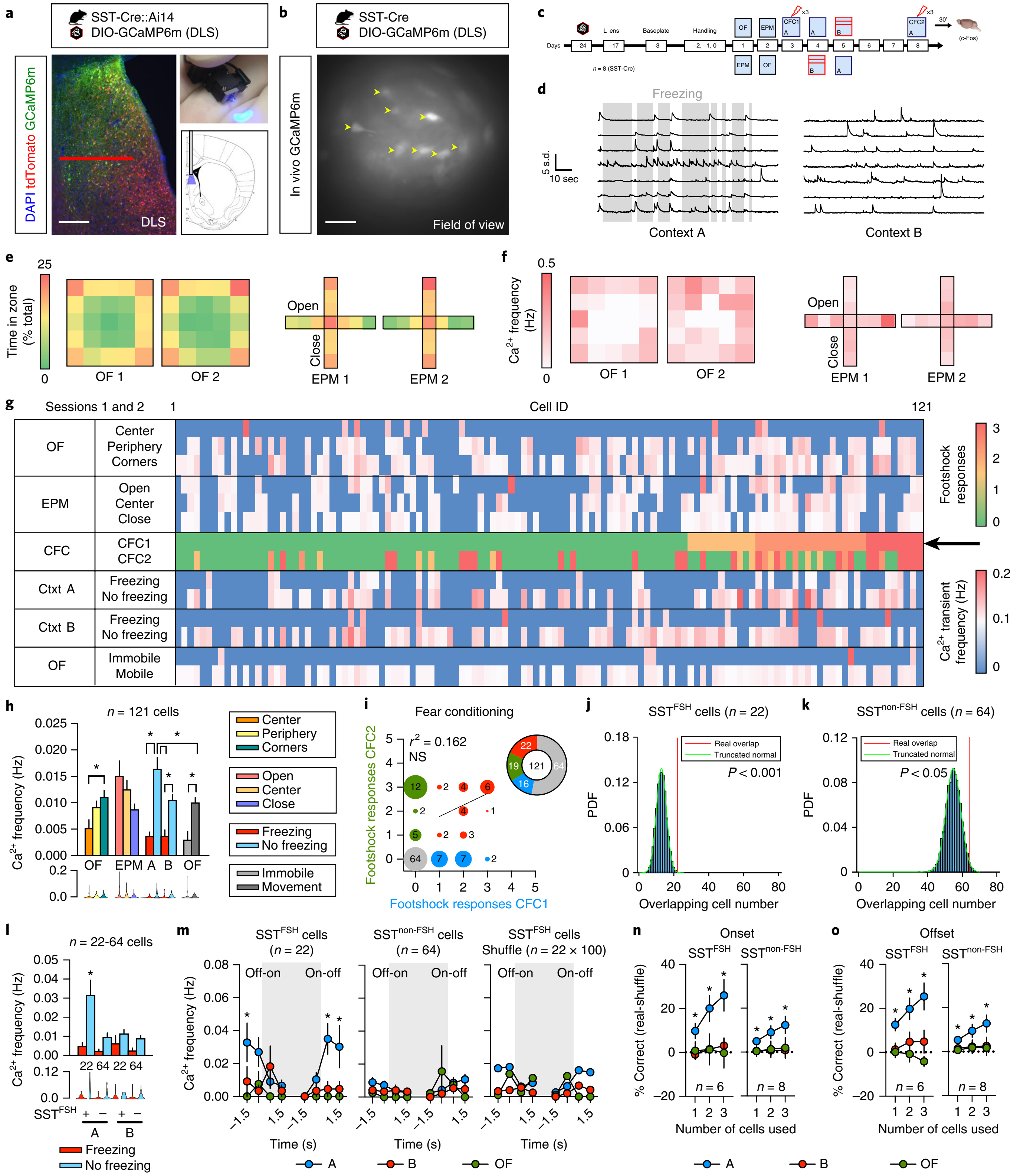

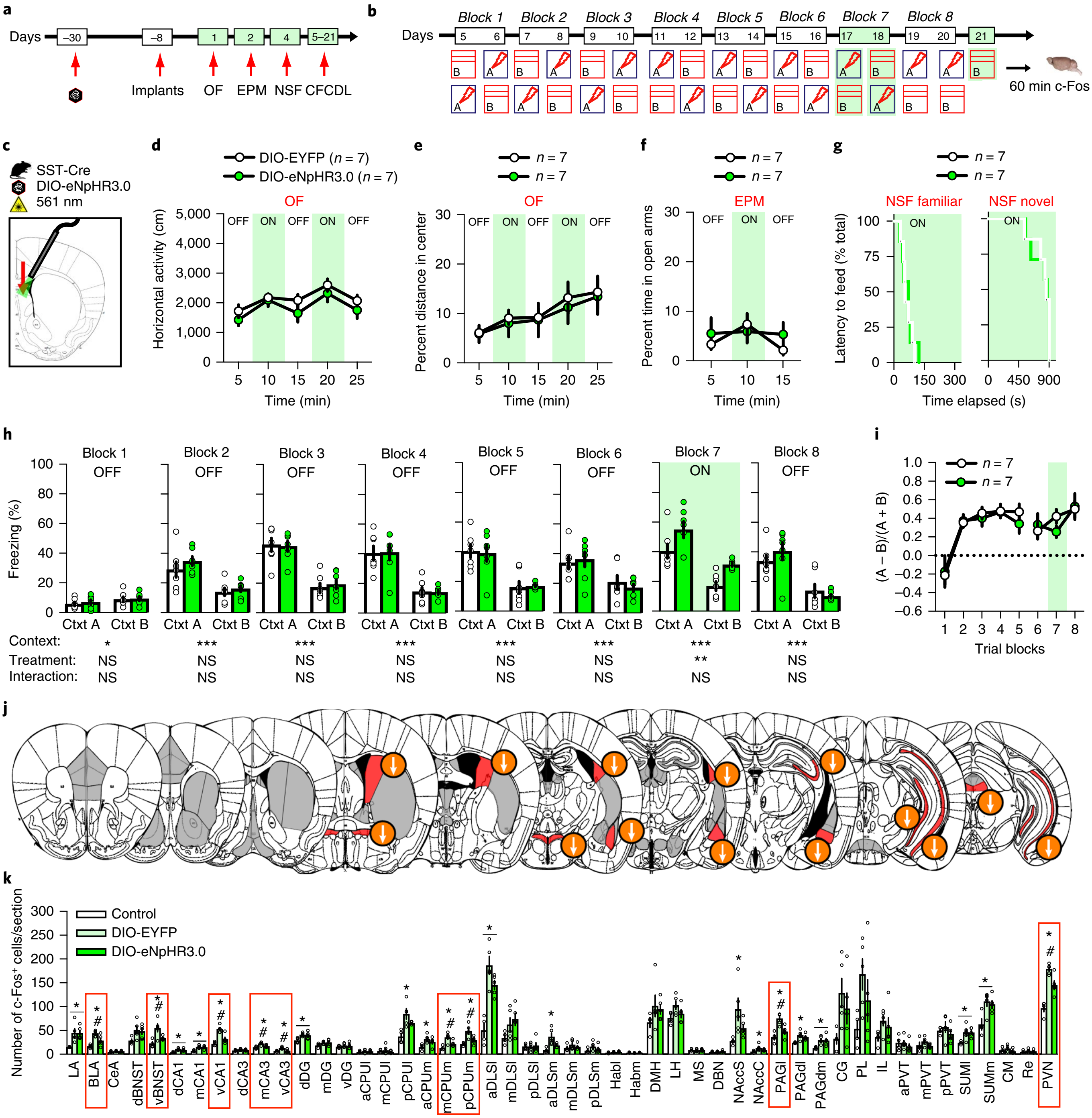

Fig. 4 | Optogenetic silencing of DLS SST-INs increases contextual fear responses. **a**,**b**, Schematic of behavioral testing timeline. **c**, Schematic illustrating infection of SST DLS-INs with DIO-eNpHR3.0 and fiber optic implantation on top of DLS in SST-Cre mice. **d**–**g**, Silencing SST cell bodies in DLS (constant illumination) has no effect on locomotor behavior and innate anxiety in OF (**d**,**e**) and EPM (**f**) and novelty suppressed feeding (NSF) (**g**). Means ± s.e.m.; $n = 7$, 7 mice per group, mixed factor two-way ANOVA. **h**, Silencing SST cell bodies (constant illumination) increases freezing behavior in contexts A and B on block training 7. Means ± s.e.m.; $n = 7$, 7 mice per group, mixed factor two-way ANOVA (repeated measure over time) followed by Bonferroni's multiple comparisons post hoc test. NS, not significant. **i**, Silencing SST cell bodies (constant illumination) did not alter fear discrimination ratio. Means ± s.e.m.; $n = 7$, 7 mice per group, mixed factor two-way ANOVA (repeated measure over time). **j**, Schematic representation of the effect of light silencing of SST cell bodies in DLS on brain-wide c-Fos expression 60 min following exposure to context B (day 21). Regions highlighted in red denote a significant effect of DIO-eNpHR3.0 and arrows indicate the direction of the effect. **k**, Detailed c-Fos immunostaining quantifications. Brain regions highlighted with red boxes indicate a significant effect of DIO-eNpHR3.0. Means ± s.e.m.; $n = 4$, 5, 5 mice per group, one-way ANOVA followed by Tukey's multiple comparisons post hoc test. $^*P < 0.05$, DIO-EYFP or DIO-eNpHR3.0 versus controls; $\#P < 0.05$, DIO-EYFP versus DIO-eNpHR3.0. All statistics are detailed in Supplementary Table 1.

oscillations are relayed to downstream subcortical brain regions[11,12]. Because hippocampal theta oscillations have been associated with various processes including freezing behavior in CA1[43], the DLS could therefore be a critical node for translating hippocampal representations into actions (such as freezing behavior). Consistently, hippocampo-septal projections are necessary for hippocampal theta

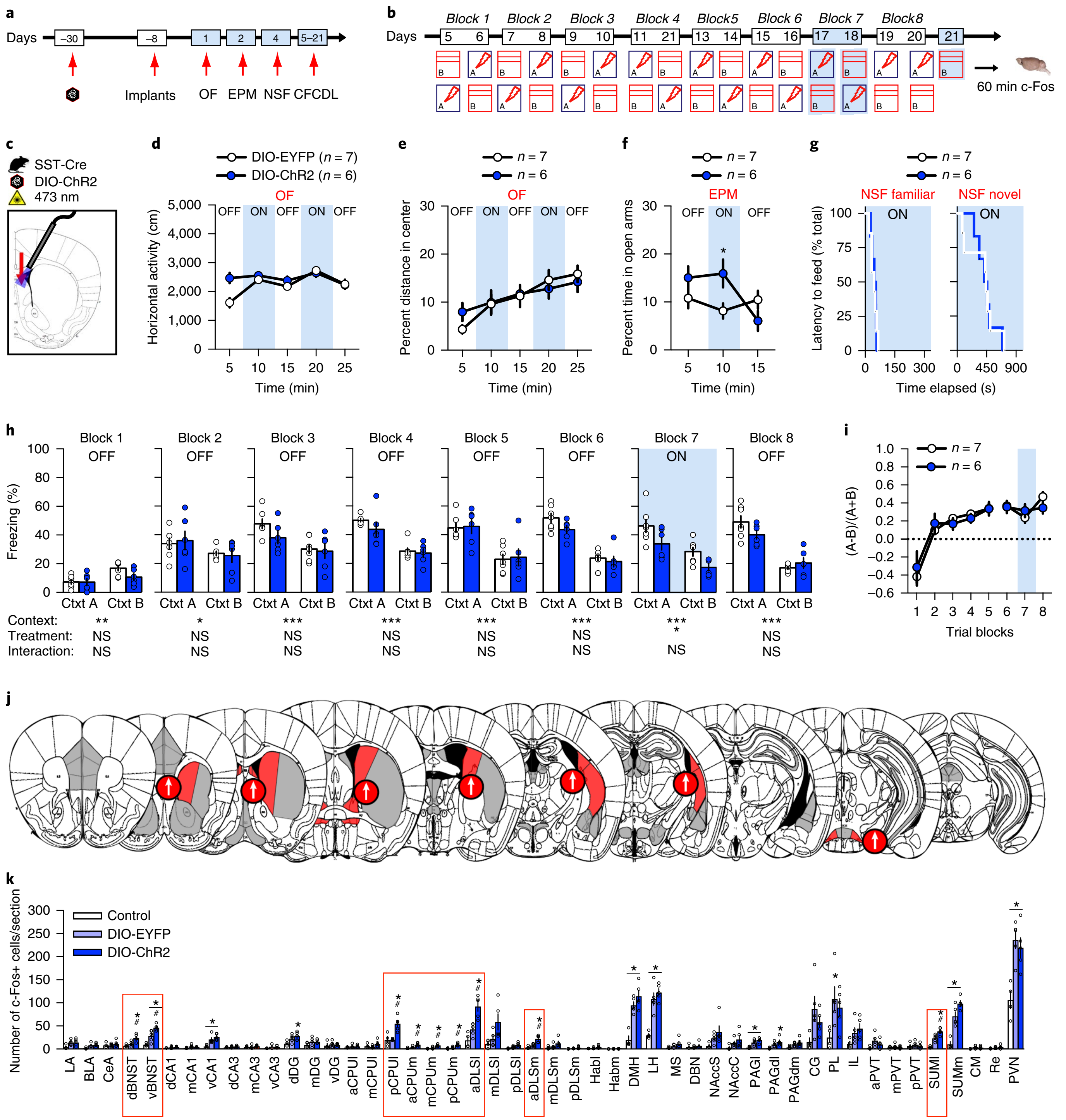

Fig. 5 | Optogenetic stimulation of DLS SST-INs attenuates anxiety and contextual fear responses. a,**b**, Schematic of behavioral testing timeline. **c**, Schematic illustrating infection of SST DLS-INs with DIO-ChR2 and fiber optic implantation on top of DLS in SST-Cre mice. **d–g**, Stimulating SST cell bodies in DLS (15 Hz) increases the time spent exploring the open arms in the EPM (**f**) but has no effect on locomotor behavior and innate anxiety in OF (**d**,**e**) and novelty suppressed feeding (NSF) (**g**). Means ± s.e.m.; $n = 7$, 6 mice per group, mixed factor two-way ANOVA followed by Bonferroni's multiple comparisons post hoc test. *$P < 0.05$, DIO-EYFP versus DIO-ChR2 (**f**). **h**, Stimulating SST cell bodies (15 Hz) decreases freezing behavior in contexts A and B on block training 7. Means ± s.e.m.; $n = 7$, 6 mice per group, mixed factor two-way ANOVA (repeated measure over time). **i**, Stimulating SST cell bodies (15 Hz) did not alter fear discrimination ratio. Means ± s.e.m.; $n = 7$, 6 mice per group, mixed factor two-way ANOVA (repeated measure over time). **j**, Schematic representation of the effect of light stimulation of SST cell bodies in DLS on brain-wide c-Fos expression 60 min after exposure to context B (day 21). Regions highlighted in red denote a significant effect of DIO-ChR2, and arrows indicate the direction of the effect. **k**, Detailed c-Fos immunostaining quantifications. Brain regions highlighted with red boxes indicate a significant effect of DIO-ChR2. Means ± s.e.m.; $n = 4$, 5, 5 mice per group, one-way ANOVA followed by Tukey's multiple comparisons post hoc test. *$P < 0.05$, DIO-EYFP or DIO-ChR2 versus controls; #$P < 0.05$, DIO-EYFP versus DIO-ChR2. All statistics are detailed in Supplementary Table 1.

oscillation induced decrease in ambulatory behavior[11], and direct theta stimulation of DLS inhibitory projections to LH is sufficient to decrease ambulatory behavior[11]. These data suggest that theta oscillations throughout hippocampo-septal and subcortical brain regions enable an increase in defensive responses upon exposure to a context associated with footshocks. We therefore hypothesize that SST-IN activity may uncouple theta oscillations within such a network in order to release the brakes on mobility. Interestingly, activity of a subpopulation of SST-INs in the hippocampus was found to positively correlate with mobility[44]. These SST-INs receive inputs from GABAergic projections arising in the medial septum that contribute to regulation of mobility and as such, may modulate DLS $\mathrm{SST^{FSH}}$ and $\mathrm{SST^{non\text{-}FSH}}$ cell activity via their actions on CA3 neurons.

Single-unit recordings in the lateral septum had identified a population of cells whose activity positively tracked the animal's activity in the open arms of the EPM[28]. Our studies identify SST-INs as one such population. Optogenetic stimulation of DLS SST-INs increased time in the open arms of the EPM. Because SST is inhibitory[45] and SST infusions into the DLS also increased exploration in the open arms of the EPM (in rats[46]), it is plausible that DLS SST-INs disinhibit other DLS-INs to produce anxiolytic effects in the EPM. The identification of specific markers for the DLS SST-IN subpopulations that we have identified will permit assessment of contributions of distinct DLS SST-IN subpopulations on behavioral motifs operational during different conflict-based paradigms for anxiety[47].

In conclusion, our studies identify previously underappreciated functional heterogeneity in DLS SST-INs and suggest a role for a stable, potentially hardwired population of DLS SST-INs as sensors of conditioned threat and arbiters of mobility that calibrate context appropriate behavioral fear responses.

Online content

Any methods, additional references, Nature Research reporting summaries, source data, statements of data availability and associated accession codes are available at https://doi.org/10.1038/s41593-018-0330-y.

Received: 22 August 2017; Accepted: 17 December 2018;

References

1. Likhtik, E. & Gordon, J. A. Circuits in sync: decoding theta communication in fear and safety. *Neuropsychopharmacology* **39**, 235–236 (2014).
2. Mahan, A. L. & Ressler, K. J. Fear conditioning, synaptic plasticity and the amygdala: implications for posttraumatic stress disorder. *Trends Neurosci.* **35**, 24–35 (2012).
3. Risold, P. Y. & Swanson, L. W. Structural evidence for functional domains in the rat hippocampus. *Science* **272**, 1484–1486 (1996).
4. Risold, P. Y. & Swanson, L. W. Connections of the rat lateral septal complex. *Brain Res. Rev.* **24**, 115–195 (1997).
5. Sheehan, T. P., Chambers, R. A. & Russell, D. S. Regulation of affect by the lateral septum: implications for neuropsychiatry. *Brain Res. Rev.* **46**, 71–117 (2004).
6. Risold, P. Y. & Swanson, L. W. Chemoarchitecture of the rat lateral septal nucleus. *Brain Res. Rev.* **24**, 91–113 (1997).
7. Zhao, C., Eisinger, B. & Gammie, S. C. Characterization of GABAergic neurons in the mouse lateral septum: a double fluorescence in situ hybridization and immunohistochemical study using tyramide signal amplification. *PLoS One* **8**, e73750 (2013).
8. Luo, A. H., Tahsili-Fahadan, P., Wise, R. A., Lupica, C. R. & Aston-Jones, G. Linking context with reward: a functional circuit from hippocampal CA3 to ventral tegmental area. *Science* **333**, 353–357 (2011).
9. Calandreau, L., Desgranges, B., Jaffard, R. & Desmedt, A. Switching from contextual to tone fear conditioning and vice versa: the key role of the glutamatergic hippocampal-lateral septal neurotransmission. *Learn. Mem.* **17**, 440–443 (2010).
10. Thomas, E., Yadin, E. & Strickland, C. E. Septal unit activity during classical conditioning: a regional comparison. *Brain Res.* **547**, 303–308 (1991).
11. Bender, F. et al. Theta oscillations regulate the speed of locomotion via a hippocampus to lateral septum pathway. *Nat. Commun.* **6**, 8521 (2015).
12. Tingley, D. & Buzsáki, G. Transformation of a spatial map across the hippocampal-lateral septal circuit. *Neuron* **98**, 1229–1242.e5 (2018).
13. Anthony, T. E. et al. Control of stress-induced persistent anxiety by an extra-amygdala septohypothalamic circuit. *Cell* **156**, 522–536 (2014).
14. Guzmán, Y. F. et al. Fear-enhancing effects of septal oxytocin receptors. *Nat. Neurosci.* **16**, 1185–1187 (2013).
15. Menon, R. et al. Oxytocin signaling in the lateral septum prevents social fear during lactation. *Curr. Biol.* **28**, 1066–1078.e6 (2018).
16. Shin, S. et al. Drd3 signaling in the lateral septum mediates early life stress-induced social dysfunction. *Neuron* **97**, 195–208.e6 (2018).
17. McHugh, T. J. et al. Dentate gyrus NMDA receptors mediate rapid pattern separation in the hippocampal network. *Science* **317**, 94–99 (2007).
18. Sahay, A. et al. Increasing adult hippocampal neurogenesis is sufficient to improve pattern separation. *Nature* **472**, 466–470 (2011).
19. Besnard, A., Laroche, S. & Caboche, J. Comparative dynamics of MAPK/ERK signalling components and immediate early genes in the hippocampus and amygdala following contextual fear conditioning and retrieval. *Brain Struct. Funct.* **219**, 415–430 (2014).
20. Wheeler, A. L. et al. Identification of a functional connectome for long-term fear memory in mice. *PLoS Comput. Biol.* **9**, e1002853 (2013).
21. Fanselow, M. S. & Dong, H. W. Are the dorsal and ventral hippocampus functionally distinct structures? *Neuron* **65**, 7–19 (2010).
22. Kim, Y. et al. Brain-wide maps reveal stereotyped cell-type-based cortical architecture and subcortical sexual dimorphism. *Cell* **171**, 456–469.e22 (2017).
23. Wickersham, I. R., Finke, S., Conzelmann, K. K. & Callaway, E. M. Retrograde neuronal tracing with a deletion-mutant rabies virus. *Nat. Methods* **4**, 47–49 (2007).
24. Sun, Y. et al. Cell-type-specific circuit connectivity of hippocampal CA1 revealed through Cre-dependent rabies tracing. *Cell Reports* **7**, 269–280 (2014).
25. Seidler, B. et al. A *Cre-loxP*-based mouse model for conditional somatic gene expression and knockdown in vivo by using avian retroviral vectors. *Proc. Natl Acad. Sci. USA* **105**, 10137–10142 (2008).
26. Resendez, S. L. et al. Visualization of cortical, subcortical and deep brain neural circuit dynamics during naturalistic mammalian behavior with head-mounted microscopes and chronically implanted lenses. *Nat. Protoc.* **11**, 566–597 (2016).
27. Chen, T. W. et al. Ultrasensitive fluorescent proteins for imaging neuronal activity. *Nature* **499**, 295–300 (2013).
28. Thomas, E., Burock, D., Knudsen, K., Deterding, E. & Yadin, E. Single unit activity in the lateral septum and central nucleus of the amygdala in the elevated plus-maze: a model of exposure therapy? *Neurosci. Lett.* **548**, 269–274 (2013).
29. Frankland, P. W., Cestari, V., Filipkowski, R. K., McDonald, R. J. & Silva, A. J. The dorsal hippocampus is essential for context discrimination but not for contextual conditioning. *Behav. Neurosci.* **112**, 863–874 (1998).
30. Strange, B. A., Witter, M. P., Lein, E. S. & Moser, E. I. Functional organization of the hippocampal longitudinal axis. *Nat. Rev. Neurosci.* **15**, 655–669 (2014).
31. Bannerman, D. M. et al. Regional dissociations within the hippocampus–memory and anxiety. *Neurosci. Biobehav. Rev.* **28**, 273–283 (2004).
32. Kheirbek, M. A. et al. Differential control of learning and anxiety along the dorsoventral axis of the dentate gyrus. *Neuron* **77**, 955–968 (2013).
33. Besnard, A. & Sahay, A. Adult hippocampal neurogenesis, fear generalization, and stress. *Neuropsychopharmacology* **41**, 24–44 (2016).
34. Guo, N. et al. Dentate granule cell recruitment of feedforward inhibition governs engram maintenance and remote memory generalization. *Nat. Med.* **24**, 438–449 (2018).
35. Raam, T., McAvoy, K. M., Besnard, A., Veenema, A. H. & Sahay, A. Hippocampal oxytocin receptors are necessary for discrimination of social stimuli. *Nat. Commun.* **8**, 2001 (2017).
36. Roy, D. S. et al. Distinct neural circuits for the formation and retrieval of episodic memories. *Cell* **170**, 1000–1012.e19 (2017).
37. Cai, D. J. et al. A shared neural ensemble links distinct contextual memories encoded close in time. *Nature* **534**, 115–118 (2016).
38. Carus-Cadavieco, M. et al. Gamma oscillations organize top-down signalling to hypothalamus and enable food seeking. *Nature* **542**, 232–236 (2017).
39. Kepecs, A. & Fishell, G. Interneuron cell types are fit to function. *Nature* **505**, 318–326 (2014).
40. Dehorter, N. et al. Tuning of fast-spiking interneuron properties by an activity-dependent transcriptional switch. *Science* **349**, 1216–1220 (2015).
41. Gielow, M. R. & Zaborszky, L. The input-output relationship of the cholinergic basal forebrain. *Cell Reports* **18**, 1817–1830 (2017).
42. Poulin, J. F., Tasic, B., Hjerling-Leffler, J., Trimarchi, J. M. & Awatramani, R. Disentangling neural cell diversity using single-cell transcriptomics. *Nat. Neurosci.* **19**, 1131–1141 (2016).
43. Seidenbecher, T., Laxmi, T. R., Stork, O. & Pape, H. C. Amygdalar and hippocampal theta rhythm synchronization during fear memory retrieval. *Science* **301**, 846–850 (2003).

44. Arriaga, M. & Han, E. B. Dedicated hippocampal inhibitory networks for locomotion and immobility. *J. Neurosci.* **37**, 9222–9238 (2017).
45. Urban-Ciecko, J. & Barth, A. L. Somatostatin-expressing neurons in cortical networks. *Nat. Rev. Neurosci.* **17**, 401–409 (2016).
46. Yeung, M. & Treit, D. The anxiolytic effects of somatostatin following intra-septal and intra-amygdalar microinfusions are reversed by the selective sst2 antagonist PRL2903. *Pharmacol. Biochem. Behav.* **101**, 88–92 (2012).
47. Markowitz, J. E. et al. The striatum organizes 3D behavior via moment-to-moment action selection. *Cell* **174**, 44–58.e17 (2018).

Acknowledgements

We thank Y. Ziv, C. Harvey, M. Kheirbek and members of the Sahay lab for their comments on the manuscript. A.B. acknowledges support from 2014 NARSAD Young Investigator Award, Bettencourt-Schueller Foundation, Philippe Foundation and 2016 MGH ECOR Fund for Medical Discovery (FMD) Postdoctoral Fellowship Awards. W.F. was supported by 2013 HSCI Harvard Internship Program Award. A.R. was supported by 2017 HSCI Harvard Internship Program Award. A.S. acknowledges support from the NIH Biobehavioral Research Awards for Innovative New Scientists (BRAINS; grant R01MH104175), NIH–R01AG048908, NIH-1R01MH111729, the Ellison Medical Foundation New Scholar in Aging, the Whitehall Foundation, an Inscopix Decode award, a NARSAD Independent Investigator Award, Ellison Family Philanthropic support, the Blue Guitar Fund, a Harvard Neurodiscovery Center–MADRC Center Pilot Grant award, Alzheimer's Association Research Grant, a Harvard Stem Cell Institute Development grant and HSCI seed grant.

Author contributions

A.B., Y.G., M.T.K., H.T., A.K.R., T.L., W.F., and I.D. performed experiments. X.X., D.S. and L.S.Z. contributed reagents. A.S. and A.B. codeveloped the concept, analyzed data and wrote the manuscript. A.S. conceived the project and supervised all aspects of the project.

Competing interests

The authors declare no competing interests.

Additional information

Supplementary information is available for this paper at https://doi.org/10.1038/s41593-018-0330-y.

Reprints and permissions information is available at www.nature.com/reprints.

Correspondence and requests for materials should be addressed to A.S.

Publisher's note: Springer Nature remains neutral with regard to jurisdictional claims in published maps and institutional affiliations.

Methods

Animal care. Male mice were housed four per cage in a 12 h (7:00 a.m. to 7:00 p.m.) light/dark colony room at 22 °C–24 °C with ad libitum access to food and water. Age-matched, male mice (2–4 months old) were used for behavioral experiments. Cagemates were randomly assigned to groups prior to virus injections. Behavioral experiments took place between 8:00 a.m. and 6:00 p.m. All animals were handled, and experiments were conducted in accordance with procedures approved by the Institutional Animal Care and Use Committee at the Massachusetts General Hospital and Boston University in accordance with NIH guidelines.

Blinding. During testing, investigators were not blind to condition. However, results were replicated across several cohorts. Videos for behavioral scoring (that is, freezing behavior) were analyzed using FreezeView softwares (Actimetrics, Wilmette, IL) during sessions without light application. For sessions in which mice received photostimulation (silencing), the light coming out of the implants prevented automatic scoring and was therefore independently scored by two investigators. Other analyses of behavior such as ambulation in the OF was scored automatically using MotorMonitor Software (Kinder Scientific, Poway, CA). Anxiety assessment in the elevated plus maze and novelty suppressed feeding tests were carried out by one investigator blinded to treatment and/or genotype. A. Sahay (PI) selected individuals in the lab to perform independent scoring.

Statistical analysis. No statistical methods were used to predetermine sample sizes, but our sample sizes are similar to those reported in previous publications[48–51]. Statistical analysis was carried out using GraphPad Prism v7 software. Data (means ± s.e.m.) were analyzed using paired or unpaired two-tailed Student's *t* test, ordinary one-way ANOVA (with or without repeated measures over time) followed by Tukey's multiple comparisons test when appropriate (difference among means, $P < 0.05$), mixed factor two-way ANOVA (with or without repeated measures over time) followed by Bonferroni's multiple comparisons test when appropriate (only if interaction, $P < 0.05$). Multiple comparisons for correlation matrix data were corrected with Bonferroni's correction method. Novelty suppressed feeding data were analyzed using a log-rank (Mantel Cox) test. Statistical comparison between experimental overlap of active cells across Ca^{2+} imaging sessions with a truncated null distribution was performed with one-sample *z* test. Data distribution was assumed to be normal, but this was not formally tested unless specified otherwise. Detailed statistical analyses can be found in Supplementary Table 1. In any case, significance was set at $P < 0.05$.

Mouse lines. 8-week-old C57BL/6J male mice were purchased from Jackson Laboratories (Bar Harbor, ME). *Rosa-CAG-LSL-tdTomato-WPRE::deltaNeo* (Ai14) (C57BL/6J) mouse line harbors a *loxP*-flanked STOP cassette, allowing transcription of CAG promoter-driven tdTomato following Cre-mediated recombination[52]. Ai14 was purchased from Jackson labs (stock number 007914). *Sst-IRES-Cre* knock-in (C57BL/6J) mouse line expresses Cre recombinase in somatostatin-expressing neurons[53]. *SST-IRES-Cre* was purchased from Jackson labs (stock number 028864). *Gad2-IRES-Cre* knock-in (C57BL/6J) mouse line expresses Cre recombinase in GAD2-expressing neurons[53]. *Gad2-IRES-Cre* was purchased from Jackson labs (stock number 028867). *Rosa-LSL-Tva-lacZ* (mixed 129S6;C57BL/6J) mouse line has a *loxP*-flanked STOP cassette allowing transcription of avian receptor Tva-lacZ fusion gene following Cre-mediated recombination[25]. *Rosa-LSL-TVA-lacZ* mouse line was generously provided by D.S. Tail DNA from all offspring was genotyped via PCR to detect the presence of each transgene separately. All experiments were conducted with 8- to 16-week-old mice (unless indicated otherwise).

Contextual fear conditioning discrimination learning. The conditioning chambers (18 × 18 × 30 cm) consisted of two clear Plexiglas walls and ceiling, two metal walls, and a stainless steel grid floor (Coulbourn Instruments, Whitehall, PA). The conditioning chambers were placed inside a ventilated, sound-dampening isolation cubicles and lit by house lights mounted on one wall (Coulbourn Instruments, Whitehall, PA). FreezeFrame and FreezeView softwares (Actimetrics, Wilmette, IL) were used for recording and analyzing freezing behavior, respectively. For the training context (designated 'A' throughout), the cubicle door was closed, the fan and house light were on, a light cue was on, stainless-steel bars were exposed, silver wall panels were used, and each conditioning chamber was cleaned with 70% ethanol between each trial. Context B was a modified version of context A by covering the stainless-steel bars with a solid floor covered with bedding, using black wall panels (covering 30% of total wall surface), with 15-cm-high curved green plastic inserts covering the bottom half of the walls, and the house fan and lights turned off. The cubicle door was left ajar, and white noise was delivered through built-in speakers for the duration of the testing. The bedding was changed between trials. The contextual fear conditioning protocol consisted of delivering a single 2 s footshock of 0.7 mA 180 s after placement of the mouse in the training context A. The mouse was taken out 20 s after termination of the footshock. No footshock was administered in context B during 180 s sessions. Mice were allowed to rest for 2–3 h between tests. Freezing behavior over the initial 180 s was used to assess discrimination between both contexts. The discrimination ratio was calculated as (freezing in training context − freezing in similar context) / (freezing in training context + freezing in similar context).

In the first experiment (Fig. 1), CFCDL consisted of five block trainings (10 d). Two groups of mice were trained to discriminate between contexts A and B or contexts A and context A′. Context A′ consisted of a slightly modified version of context A, with 15-cm-high curved transparent plastic inserts covering the bottom half of the walls, the light cue off and mouse bedding covering the bottom of the conditioning chamber placed underneath the stainless-steel bars. At the end of CFCDL, a final exposure to context A′ or B (day 11) took place 60 min (or 30 min, Supplementary Fig. 1a) prior to sacrifice for c-Fos brain-wide analysis (no footshock delivered on day 11).

In the second experiment (Supplementary Fig. 2f), CFCDL was carried out as described in Fig. 1 with the exception that two other groups were trained following the exact same schedule, but no footshocks were delivered throughout conditioning. At the end of CFCDL, a final exposure to context A or B (day 11) took place 60 min prior to sacrifice for c-Fos analysis in DLS (no footshock delivered on day 11).

AAV, rabies and canine virus construction and packaging. AAV-DJ-EF1α -DIO-GCaMP6m-WPRE (5.2×10^{12} particles/mL) was packaged by Stanford Gene Vector and Virus Core (Stanford, CA). The recombinant AAV5-EF1a-DIO-eYFP-WPRE-hGH (5.8×10^{12} particles/mL), AAV5-EF1a-DIO-eNpHR3.0-WPRE-hGH (6×10^{12} particles/mL) and AAV5-EF1a-DIO-hChR2(H134R)-eYFP-WPRE-hGH (6.2×10^{12} particles/mL) were packaged by the University of Pennsylvania Vector Core (Philadelphia, PA). The recombinant AAV5-CaMKIIα-hChR2(H134R)-eYFP (4×10^{12} particles/mL) was packaged by the University of North Carolina Vector Core (Chapel Hill, NC). AAV8-EF1a-FLEX-HB (2×10^{11} particles/mL) and pseudotyped RG-deleted rabies virus EnvA-SADΔG-mCherry (2×10^{9} particles/mL) were kindly provided by X.X. Canine-associated virus-2 encoding Cre recombinase (2×10^{10} particles/mL) was kindly provided by L.S.Z.

Viral stereotactic surgery. Adult mice (8 weeks old) were maintained under standard housing conditions; mice were given carprofen (5 mg/kg, subcutaneously, Patterson Veterinary Supply, Devens, MA) prior to surgery and 24 h later to minimize discomfort. Mice were anaesthetized with ketamine and xylazine (10 mg/mL and 1.6 mg/mL, intraperitoneally, Patterson Veterinary Supply, Devens, MA) and placed in a stereotaxic frame (Stoelting, Holliston, MA). Small holes were drilled at each injection location and injected with a Hamilton microsyringe at a rate of 0.1 µl/min. Viruses were injected into anterior dorsolateral septum (flat skull ± 0.25 mm ML, +1.15 mm AP, −3 mm DV from bregma) of Gad2-Cre or SST-Cre mice (0.2 µl, bilateral, 4 weeks for AAV5-EF1a-DIO-eYFP, AAV5-EF1a-DIO-eNpHR3.0-eYFP or AAV5-EF1a-DIO-ChR2-eYFP; 0.5 µl, unilateral, 3.5 weeks for AAV-DJ-EF1α-DIO-GCaMP6m-WPRE). Canine2-Cre virus was injected into posterior dorsolateral septum (flat skull ± 0.4 mm ML, +0.0 mm AP, −2.8 mm DV from bregma) of Ai14 mice (0.5 µl, bilateral, 2 weeks). Viruses were injected into posterior dorsolateral septum (flat skull ± 0.4 mm ML, +0.0 mm AP, −2.8 mm DV from bregma) of SST-Cre::TVA mice (0.5 µl, unilateral, 3weeks for AAV8-EF1a-FLEX-HB followed by 0.5 µl, unilateral, 10 days for EnvA-SADΔG-mCherry). Viruses were injected into dorsal CA3 (± 2.5 mm ML, −2.1 mm AP, −2.25 mm DV from bregma) of SST-Cre::Ai14 mice (0.5 µl, bilateral, 4 weeks for AAV5-CaMKIIα -ChR2-eYFP). After completion of the injection, the needle was left on the site of injection for 5 min, raised 0.2 mm and left on the site for an additional 5 min to allow diffusion of virus at the injection site and then slowly withdrawn. The skin incision was closed carefully using nylon sutures. Behavioral and ex vivo electrophysiological experiments were conducted 4–5 weeks following surgery (except for rabies tracing analysis which took place 10 days after EnvA-SADΔ G-mCherry infection).

Microendoscope implantation. 1 week after AAV-DJ-EF1α-DIO-GCaMP6m-WPRE injection, we performed a second surgery to implant a GRIN lens microendoscope probe (0.5 mm Diameter, 6.1 mm length, Inscopix, Palo Alto, CA) into anterior dorsolateral septum (flat skull ± 0.25 mm ML, +1.15 mm AP, −2.7 mm DV from bregma). GRIN lens implantation was conducted into the craniotomy previously achieved during viral surgery. Prior to implantation, a scored three holes straight plate (Part: 503617, World Precision instruments, Sarasota, FL) was sealed onto the skull with super glue (Part: LOC1364076, Loctite), whose center hole was located on top of the craniotomy. Three bone anchor screws (Part: MD1310, Bioanalytical Systems, West Lafayette, IN) were attached to the skull, one anterior (approximately +2.0 mm AP from bregma) and two posterior to the straight plate (approximately −2.0 mm AP from bregma). GRIN lens implantation was achieved at a rate of 0.2 mm/min. The GRIN lens was then attached with dental cement dyed with black nail polish applied into the well formed by the straight plate hole around the GRIN lens. Once the GRIN lens was firmly attached, black dyed dental cement was applied over the cranium, around the screws and the straight plate. Mice recovered for 2 weeks and a miniature baseplate (Inscopix, Palo Alto, CA) was subsequently attached to the cranium allowing the connection to a miniature microscope (nVista HD, Inscopix, Palo Alto, CA). The optimal working distance between the GRIN lens and the projection image of the cells outside the lens was approximately +500 µm from the top of the lens. Previous pilot experiments also indicated dental cement shrinkage of approximately 200 µm. Thus, the baseplate of the miniature microscope was attached to the cranium at approximately +700 µm with dental cement dyed with black nail polish. Once the dental cement hardened, the microscope was detached and the mouse was placed back into its home cage (mice were housed two per cage with a separator).

Mouse behavior and calcium imaging. Prior to behavioral testing, mice were habituated to the miniature microscope attachment for 3 consecutive days. On day 1, behavioral exploration was monitored over 3 min calcium imaging sessions in the open-field (OF) and elevated plus maze EPM (2 h apart).

The OF consisted in a Plexiglas box of 41 × 41 cm (Kinder Scientific, Poway, CA) and the EPM consisted of a black Plexiglas apparatus (Med Associates Inc., St. Albans, VT) placed 1 m above the floor, with two open arms (67 cm × 7 cm) perpendicular to two enclosed arms (67 × 7 × 17 cm). The four arms were separated by a neutral transition central square (5 × 5 cm) in which mice were placed at the beginning of the experiment and their behavior was recorded for 15 min with a video camera system (ViewPoint, Lyon, France) located above the maze. On day 2, behavioral exploration was monitored over 3 min calcium imaging sessions in the EPM and OF (2 h apart). On day 3, mice were trained in the CFC (CFC1) over a 3 min calcium imaging session during which they received 3 footshocks in context A (footshocks delivered at 30, 90 and 150 sec). On day 4, freezing behavior was measured during 3 min calcium imaging sessions in context A and safe context B (2 h apart). On day 4, freezing behavior was measured during 3 min calcium imaging sessions in context B and A (2 h apart). On day 8, mice were retrained in the CFC (CFC2) over a 3 min calcium imaging session during which they received 3 footshocks in context A 30 min prior to sacrifice for c-Fos analysis.

Calcium imaging using the miniature microscope. Before each calcium imaging session, the miniature microscope was briefly attached to its baseplate in a transition cage filled with bedding. Animals were allowed to habituate to this procedure for 3 consecutive days before the onset of the behavioral experiments. Each session involved 3 min of calcium imaging across a field-of-view of approximately 300 µm x 300 µm, which matched that seen in any previous sessions in the same animal. After each session the microscope was detached and the mouse returned to its home cage.

Fluorescence calcium imaging videos were streamed directly to a hard disk, obtained using 140 µW of LED illumination intensity and 12 bit images (1,000 × 1,000 pixels) were acquired at a frame rate of 20 Hz (50 ms exposure). At the end of each experiment (on day 8), GCaMP6m expression and GRIN lens implantation was histologically controlled in the DLS.

Basic processing of the calcium imaging videos. Fluorescence calcium imaging videos were analyzed using Inscopix Data Processing Software (v1.0.0.2273, Inscopix, Palo Alto, CA). Prior to further processing and analysis, videos were preprocessed by fixing defective pixels and row noise as well as motion correction.

Image Processing with PCA-ICA. After motion correction, each image frame was re-expressed in units of relative changes in fluorescence, $\Delta F(t)/F0 = (F(t) - F0)/F0$, where F0 is the mean image obtained by averaging the entire video. Spatial filters corresponding to individual neurons were identified using Inscopix Data Processing Software (v1.0.0.2273, Inscopix, Palo Alto, CA) based on principal and independent component analyses[54]. Cells spatial filters were identified based on the calcium data acquired over the entire session. For each filter, all pixels were then zeroed with values < 50% of that filter's maximum intensity. To obtain time traces of calcium activity, each cell thresholded spatial filter was added to the $\Delta F(t)/F0$ movie. As previously described[55], the extracted spatial filters generally had sizes, morphologies and activity traces that were characteristic of individual neurons. Every cell included in the analyses was validated by visual inspection.

Cell registration across 10 recording sessions using Inscopix Data Processing Software (v1.0.0.2273, Inscopix, Palo Alto, CA). This corrected for potential slight translations, rotations, or focus-dependent magnification changes between sessions and yielded the location of each cell in the reference coordinate system.

Image processing (CNMF-E). After motion correction, cells were segmented using the automated algorithm Constrained Non-negative Matrix Factorization optimized for microEndoscopic data (CNMF-E)[56], using an estimated cell diameter of 33 pixels (determined from spatial image after preprocessing algorithm developed for CNMF)[57]. The putative neurons identified by CNMF-E were manually verified and merged to ensure accuracy. Raw traces were downsampled to 1 s time bins before spiking events were determined by the findpeaks function of MATLAB (Mathworks, Natick MA) using the following parameters (MinPeakProminence = 4 s.d., MinPeakDist = 2 s).

Cells were tracked across multiple imaging sessions through the software CellReg[58]. Spatial maps of segmented cells from CNMF-E were uploaded to CellReg, which then probabilistically tracked cells across multiple sessions. Two parameters are used to verify that a cell pair represents indeed the same cell or different cells. These parameters are the spatial correlation and the center of mass distance. Sheintuch et al[58] based their model on the bimodal distribution that results from plotting these parameters for multiple neurons, with one peak representing same cells and one peak representing different cells (true for both parameters). The combination of the tow parameters proved to be a reliable tool to probabilistically identify cell pairs of same cells across multiple session[58].

Cell selection method. In order to determine functional cell types based on selectivity, we categorized cells based on two criteria: 1) Are the cells highly active (Ca^{2+} activity frequency) for a specific state, and 2) Are these cells active on both recording sessions (for example Is the cell active on Open Field session 1 AND Open Field session 2).

1. Calculation of frequency for a specific state. For each cell, we defined the Ca^{2+} activity for a specific state (for example when the mouse is in the center of the open field, "Center") to be the difference between the frequency of the mouse's state of interest, $f_{interest}$, minus the other states in the same recording session (for example we categorized the entire Open Field recording session into 3 states based on the mouse's location: "Center", "Corner", and "Periphery". Therefore, we defined the Ca^{2+} activity of the "Center" state as $f_{center} - f_{corner} - f_{periphery}$).

1.1. Validating cell selectivity. The $f_{interest}$ was then compared against a null distribution to further ensure that the activity was state-specific. For each cell, we created a null distribution for each state (for example given the Open Field, for each cell we created 3 separate null distributions corresponding to each of the following states: "Center", "Corner", "Periphery"). We created null distributions by shuffling Ca^{2+} events of a cell across a single (180 s) recording session (1000 iterations). State-specific frequencies were then calculated for the null distributions. We will call these frequencies f_{null}. For example, if a cell was noted to have 10 "spikes" in a single session, these 10 spikes were randomly moved across the entire session to see what the state-specific frequency would be given random timing of events (non-selective activity/cell). We then compared $f_{interest}$ against f_{null} to determine whether a cell was selective for a specific state. If the real difference exceeded 1 SD of the null distribution, the cell was considered to be behaviorally selective. We modeled this procedure based on an existing publication[59]. In the aforementioned study, the authors were able to plot a distribution of the difference between $f_{interest}$ and f_{null} to note that the state-specific and non-specific cells had a difference of about 1 s.d. Due to the lower number of cells and lower frequency of Ca^{2+} events in our study, we decided to use the published value of 1 s.d.[59].

2. Is the cell selective in more than 1 session?. Our study design allowed us to filter for cells that are selectively active for a behavior of interest in two independent sessions. To determine if a population of state-specific cells identified in one session (as described above) was consistently active across the second behavioral recording sessions, we used the following procedure. Here, we compared the selective cells in session 1 (population N_1) to the selective cells in session 2 (population N_2). The final population of selective cells (n_{real}) results from the overlap of N_1 and N_2 ($n_{real} = N_1 \cap N_2$).

2.1 Validation of overlap in cell activity across sessions. To determine whether the population of cells was indeed consistently selective for a certain behavior, we compared n_{real} against a null distribution. We created the null distribution by iteratively resampling a mock population of the same size as N_1 from our entire sample population. In other words, if there were 10 cells in N_1, we randomly selected 10 cells, N_{mock}, out of all cells recorded across all sessions. We then calculated a mock number of overlap, n_{mock}, as the intersection between the mock and N_2, $n_{mock} = N_{mock} \cap N_2$ (10000 iterations). If the real overlap, n_{real}, exceeded 2 s.d. from the mean of the null distribution, we considered the population of cells to be consistently selective for the state of interest across two sessions. This multistep filtering provides stringent conditions to reliably identify selective cells.

Null distribution for behavioral state transition analysis. We wanted to determine whether the difference between the SST^{FSH} cells and SST$^{non\text{-}FSH}$ in their freezing/non-freezing transitions was significant. In order to do so, we compared SST^{FSH} and SST$^{non\text{-}FSH}$ against a mock population of cells that represented a random mix of both. We developed a mock population, of the same size as footshock responsive cells, by randomly sampling from the whole population of cells (100 iterations). These mock populations were then analyzed for their freezing/non-freezing transitions.

Decoder. Based off of the results from the freezing/non-freezing transitions, we asked whether the rate of Ca^{2+} event change could predict whether the animal was entering or exiting a freezing epoch. We estimated the instantaneous rate of change by calculating the linear regression within a 2.5 s window around each time point for an entire session. This generated a 170 s graph of the instantaneous rates of change. From this graph of the instantaneous rates of change, we then predicted the freezing epoch onset to occur at a local minimum and the offset to occur at a local maximum. The local minima and maxima were found using the *findpeaks* function of MATLAB using the following parameters (MinPeakHeight = 1 s.d., MinPeakProminence = 1 s.d., MinPeakDistance = 2 s). The null graph was created by shuffling the timing of all freezing epochs across an entire session. Timing of Ca^{2+} transients were then kept constant before calculating the estimated onset and offset from the null graph (1000 iterations). We sought to assess whether the efficacy of the decoder changed with the number of cells used, N_{Cells}.

For each mouse, the decoder's efficacy for N_{Cells} was determined by averaging the performance for every combination of cells (ex. Given a mouse with cells A, B, and C, the efficacy of $N_{Cells}=2$ was determined by averaging the performance of groups [A, B], [A, C], and [B, C]). The number of correct predictions by the decoder, $T_{Correct}$, was determined from the total number of actual onset/offset events, T_{Total}, as the number of predictions within 2 s of an actual onset/offset event. The efficacy was then calculated as $R_{Real}-R_{Null}$ where $R=\frac{T_{Correct}}{T_{Total}}$.

Ex vivo electrophysiology. Coronal brain slices including hippocampus and septum (300 µm thick) were prepared using a vibratome (VT1200S, Leica, Buffalo Grove, IL). To preserve tissue health in adult animals, SST-Cre::Ai14 mice were deeply anesthetized with ketamine and xylazine (100 mg/mL and 3 mg/mL, intraperitoneally, Patterson Veterinary Supply, Devens, MA) and perfused transcardially with modified artificial cerebrospinal fluid (ACSF) containing, in mM: 124 NaCl, 2.5 KCl, 1.25 NaH_2PO_4, 25 $NaHCO_3$, 75 sucrose, 10 glucose, 1.3 ascorbic acid, 0.5 $CaCl_2$ and 7 $MgCl_2$. Slices were maintained and recorded at 29.5 °C using ACSF containing: 124 mM NaCl, 3 mM KCl, 1.25 mM NaH_2PO4, 26 mM $NaHCO_3$, 20 mM sucrose, 2 mM $CaCl_2$ and 1.5 mM $MgCl_2$, continuously oxygenated with 95/5% O2/CO2. Whole cell electrodes were pulled to tip resistances of 3–5 MΩ and contained the following internal solutions: current clamp, 135 mM potassium-gluconate, 2 mM $MgCl^+$, 10 mM HEPES, 0.4 mM EGTA, 2 MgATP, 0.5 mM Na3GTP, 10 mM phosphocreatine disodium; voltage clamp, 130 mM Cs methanesulfonate, 4 mM NaCl, 10 mM HEPES, 1 mM EGTA, 25 mM TEA-OH, 5 mM QX314-Cl, 4 mM MgATP, 0.3 mM Na3GTP and 10 mM phosphocreatine disodium. Alexa Fluor-594 or -488 was added to the internal solution to confirm cell identity in targeted recordings. Slices were imaged on a two-photon imaging system (Ultima, Bruker). Photostimulation was applied using 10-ms-long full-field illumination pulses delivered by a high-power 470 nm LED (Thorlabs, Newton, NJ) positioned above the microscope's camera port. Synaptic currents were amplified using a MultiClamp 700B (Molecular Devices, Sunnyvale, CA) and acquisition was performed with custom Matlab code and a commercial digitizer system (National Instruments, Woburn, MA). Synaptic analysis was performed in Igor Pro using freely available routines (https://sites.google.com/site/tarotoolsregister/).

Construction of Optical Fibers. 200um core, 0.37 numerical aperture (NA) multimode fiber (Thorlabs, Newton, NJ) was threaded through and glued with epoxy (Thorlabs, Newton, NJ) to a 230 µm core zirconia multimode ferrule (Precision Fiber Products, Milpitas, CA), polished and cut for implantation. Optical patch cables were generated the same way, with the free end connected to a multimode FC ferrule assembly for connecting to a 1 × 2 Optical rotary joint (Doric lenses, Québec, Canada). The other end of the rotary joint was connected via a patch cable to 473 nm laser diode (OEM laser systems, Bluffdale, UT) via a non-contact style laser to fiber coupler (OZ optics, Ontario, Canada).

Fiber optics stereotactic surgery. Age-matched, male SST-Cre mice (2–3 months old) were used for all behavioral experiments. Mice were surgically implanted with fiber optic cannulas 3 weeks following rAAV5-EF1a-DIO-eYFP, rAAV5-EF1a-DIO-eNpHR3.0-eYFP or rAAV5-EF1a-DIO-ChR2(H134R)-eYFP injection, and behavioral experiments started 1 week after surgery. Mice were implanted bilaterally with chronically dwelling optical fibers targeted to dorsolateral septum (flat skull ± 1.0 mm ML angle ± 10°, + 1.15 mm AP from bregma, implants length: 2.5 mm). Optical fibers were secured with dental cement. After surgery, mice were returned to their home cage and monitored until recovery from surgery.

In vivo laser delivery. Mice were kept in a quiet room for at least 1 h before testing. Behavioral tests took place under bright lighting conditions (700 lux) and performed in the following order: open field (day 1), elevated plus maze (day 2), novelty suppressed feeding (day 4) and contextual fear conditioning (day 5–20). Prior to each experiment, mice were bilaterally attached to the patch cables via a zirconia sleeve (Precision Fiber Products, Milpitas, CA), and allowed to recover for 30–60 sec in a transition cage similar to their home cage. The patch cables were interfaced to an FC/PC rotary joint (Doric lenses, Québec, Canada), which was attached on the other end to a 561 nm or 473 nm laser diode (OEM laser systems, Bluffdale, UT). The light power at the end of the fiber tip was 15–20 mW for 561 nm light and 8–10 mW for 473 nm light (5–6 mW when pulsing at 15 Hz). The laser diode was controlled by a Master-8 stimulator (Keysight Technology, Santa Clara, CA) which delivered 20 ms blue light pulses at 15 Hz. At the end of each behavioral experiment (7 weeks following viral surgery), postmortem control of viral and fiber optics placement was carried out to ensure appropriate targeting. 1 DIO-ChR2 injected mouse was discarded out of 7 animals (Fig. 5). This animal was used as a home cage control on perfusion day (day 21) for c-Fos analysis.

Open field. Optogenetic interrogation of SST-INs in the open field (OF) was recorded for 25 min divided in five 5 min laser epochs (off–on–off–on–off) in a Plexiglas OF box of 41 × 41 cm with 16 sets of double stacked pulse-modulated infrared photobeams (Kinder Scientific, Poway, CA) equally spaced on every wall (128 total) to record *x*–*y* ambulatory movements. MotorMonitor Software (Kinder Scientific, Poway, CA) defined grid lines that divided the open field into center (25% of total area) and periphery (75% of total area), with the periphery consisting of the 10 cm closest to the wall around the entire perimeter. Dependent measures were the overall motor activity quantified as the total distance traveled (in centimeters) and the distance traveled in the center divided by total distance traveled (percentage distance in center). The apparatus was cleaned with 70% ethanol between each trial.

Elevated plus maze test. Optogenetic interrogation of SST-INs in the elevated plus maze (EPM) was recorded for 15 min divided in three 5 min laser epochs (off–on–off). The maze consisted of a black Plexiglas apparatus (Med Associates Inc., St. Albans, VT) placed 1 m above the floor, with two open arms (67 cm × 7 cm) perpendicular to two enclosed arms (67 × 7 × 17 cm). The four arms were separated by a neutral transition central square (5 × 5 cm) in which mice were placed at the beginning of the experiment and their behavior was recorded for 15 min with a video camera system (ViewPoint, Lyon, France) located above the maze. Cumulative time spent in the open and closed arms was scored manually by investigators blind to the treatment conditions and data were expressed as the time spent in open arms divided by total time in open and closed arms (percentage time in open arms). An arm visit was recorded when the mouse moved its forepaws into the arm. The apparatus was cleaned with 70% ethanol between each trial.

Novelty suppressed feeding test. Optogenetic interrogation of SST-INs in the novelty suppressed feeding test (NSF) was recorded for up to 15 min in a novel context and up to 5 min in a familiar environment during which the laser was constantly ON. Mice were food deprived in clean home cages 24 h prior to testing. Mice were weighed before food deprivation and again just before testing to assess changes in body weight (approximately 10% body weight loss). A single food pellet (familiar laboratory mouse chow) was placed on a circular piece of white filter paper (12 cm diameter) positioned in the center of a plastic arena (45 cm wide × 30 cm long × 15 cm high) with wood chip bedding covering the floor. Mice were placed in a corner of the arena and the latency to approach the pellet and beginning feeding was recorded (maximum time 15 min). Immediately upon beginning to feed, each mouse was transferred to a familiar cage and the latency to begin feeding in the familiar cage was recorded (maximum time 5 min). Droppings were removed from the arena between each trial.

Contextual fear conditioning discrimination learning. Optogenetic interrogation of SST-INs in an extended version of contextual fear conditioning discrimination learning (days 5–20) was conducted over eight block trials (2 days each) in which mice learnt to discriminate between a fearful context A and a safe context B. Both contexts were presented once a day in a counterbalanced manner in order to avoid any session order bias. Mice were given 6 untethered block trials in order to reach asymptotic levels of discrimination. Block 7 was carried out with the laser constantly ON. On block 7, the percent time freezing as well as the number of freezing bouts and their average duration was measured. A final untethered block training (Block 8) was performed prior to the last exposure to context B (day 21) with the laser on, which took place 60 min prior to sacrifice for c-Fos brain-wide analysis.

Immunohistochemistry. Mice were anesthetized with ketamine and xylazine (100 and 3 mg/kg body weight, respectively) and transcardially perfused with PBS (10 mM phosphate buffer saline, pH 7.5,) at 4 °C, followed by 4% paraformaldehyde in PBS at 4 °C. Brains were post-fixed overnight in the same solution at 4 °C, then cryoprotected in PBS sucrose (30% w/v) and stored at 4 °C before freezing in OCT on dry ice. Coronal serial sections (35 µm) were obtained using a Leica cryostat in six matched sets. Sections were stored in PBS with 0.01% sodium azide at 4 °C. On day 1, free-floating sections were rinsed three times for 10 min in 10 mM phosphate buffer saline (PBS), pH 7.5, followed by a permeabilization step 15 min in 0.2 % Triton X-100 in PBS. The sections were rinsed another three times for 10 min in PBS and 2 h with a blocking buffer (10 % natural donkey serum (NDS; w/v)). After three rinses in PBS, incubation with primary antibodies rabbit anti c-fos, Calbiochem PC38, 1:10,000 (Antibodyregistry.org: AB_2106755)(discontinued); different batches of rabbit, Santa Cruz SC52, 1:2,000–1:5,000 (Antibodyregistry.org: AB_2106783)(discontinued); rabbit anti-GFP, Life Technologies A11122, 1:500 (Antibodyregistry.org: AB_221569); chicken anti-GFP, Abcam AB13970, 1:2,000 (Antibodyregistry.org: AB_300798); mouse anti-CB, Swant 300, 1:5,000 (Antibodyregistry.org: AB_10000347); goat anti-SST, Santa Cruz SC7819, 1:400 (Antibodyregistry.org: AB_2302603); mouse anti-CR, Swant 6B3, 1:500 (Antibodyregistry.org: AB_10000320); mouse anti-PV, Millipore MAB1572, 1:2,000 (Antibodyregistry.org: AB_2174013); rabbit anti-NPY, Sigma N9528, 1:10,000 (Antibodyregistry.org: AB_260814); goat anti-Chat, Millipore AB144P, 1:400 (Antibodyregistry.org: AB_11214092); mouse anti-RGS14, UC Davis/ NIH NeuroMAB, 1:400 (Antibodyregistry.org: AB_10698026) was carried out with shaking at 4 °C overnight. On day 2, sections were rinsed three times for 10 min in PBS and incubated for 90 min with a donkey anti-rabbit, anti-mouse, anti-goat and/or anti-chicken Cy3, FITC or Cy5-coupled secondary antibody

(Jackson ImmunoResearch, 1:500). Sections were rinsed three times for 10 min in PBS before mounting in PBS and coverslipped with Fluoromount.

Interregional c-Fos correlation matrix. c-Fos immunopositive cells were quantified across 48 brain regions (5 naïve mice, 5 context B mice, 5 context A′ mice). The data were averaged for the naïve animals and subsequently normalized the naïve, Context B and context A′ data. This operation was repeated for the 48 brain regions. Context B and 5 context A′ normalized c-Fos data points ($n = 10$) were plotted for each brain region (Supplementary Table 2). Each row represents one mouse, and each column represents one brain region. The normalized data were then analyzed using a built-in package in Prism 7 for cross correlation analysis. The r value was computed for every pair of Y data sets (correlation matrix). We computed nonparamateric Spearman correlations since not all the datasets were normally distributed (D'Agostino & Pearson normality test was employed at $P < 0.05$.). Next, multiple comparisons for correlation matrix data were corrected with Bonferroni's correction method: 0.05/48 = 0.001 (48 brain regions). Thus, only the comparisons whose $P < 0.001$ were taken into consideration.

Images acquisition and analysis. Images were obtained from one set of brain sections (1/6th of the brain) for each immunostaining, except for rabies tracing analysis, which was performed on the whole brain. For single stainings (c-Fos, tdTomato, GFP, CB, SST, CR, PV, NPY, Chat,), brain regions of interest were identified at various bregma coordinates. Images were acquired bilaterally with an epifluorescence microscope (Nikon) using a 10× objective. High-resolution reconstruction was achieved by combining multiple images with overlapping fields of view (NIS Elements software). Quantifications were performed manually using an image analysis software (ImageJ 1.49 v, NIH), taking into account cells with immunofluorescence above background. For dual immunostainings, *z* stacks images were acquired bilaterally with a Nikon A1R Si confocal laser, a TiE inverted research microscope using a 20x objective. Images (1024 resolution) were acquired as 14 μM z-stacks with a step size of 2 μM. For c-Fos intensity in SST cells (Supplementary Fig. 9l–n), we measured c-Fos immunoreactivity in SST cells and expressed the data as a percentage of background in the same field of view. All analyses were performed by an investigator blinded to treatment and/or genotype.

Reporting Summary. Further information on research design is available in the Nature Research Reporting Summary linked to this article.

Data availability

The data that support the findings of this study and custom MATLAB codes are available from the corresponding author upon reasonable request.

References

48. Xu, C. et al. Distinct hippocampal pathways mediate dissociable roles of context in memory retrieval. *Cell* **167**, 961–972.e16 (2016).
49. Felix-Ortiz, A. C. et al. BLA to vHPC inputs modulate anxiety-related behaviors. *Neuron* **79**, 658–664 (2013).
50. Yu, K. et al. The central amygdala controls learning in the lateral amygdala. *Nat. Neurosci.* **20**, 1680–1685 (2017).
51. Adhikari, A. et al. Basomedial amygdala mediates top-down control of anxiety and fear. *Nature* **527**, 179–185 (2015).
52. Madisen, L. et al. A robust and high-throughput Cre reporting and characterization system for the whole mouse brain. *Nat. Neurosci.* **13**, 133–140 (2010).
53. Taniguchi, H. et al. A resource of Cre driver lines for genetic targeting of GABAergic neurons in cerebral cortex. *Neuron* **71**, 995–1013 (2011).
54. Grewe, B. F. et al. Neural ensemble dynamics underlying a long-term associative memory. *Nature* **543**, 670–675 (2017).
55. Mukamel, E. A., Nimmerjahn, A. & Schnitzer, M. J. Automated analysis of cellular signals from large-scale calcium imaging data. *Neuron* **63**, 747–760 (2009).
56. Zhou, P. et al. Efficient and accurate extraction of in vivo calcium signals from microendoscopic video data. *eLife* **7**, e28728 (2018).
57. Pnevmatikakis, E. A. et al. Simultaneous denoising, deconvolution, and demixing of calcium imaging data. *Neuron* **89**, 285–299 (2016).
58. Sheintuch, L. et al. Tracking the same neurons across multiple days in Ca^{2+} imaging data. *Cell Reports* **21**, 1102–1115 (2017).
59. Jimenez, J. C. et al. Anxiety cells in a hippocampal-hypothalamic circuit. *Neuron* **97**, 670–683.e6 (2018).

nature research

Corresponding author(s): Amar Sahay

Reporting Summary

Nature Research wishes to improve the reproducibility of the work that we publish. This form provides structure for consistency and transparency in reporting. For further information on Nature Research policies, see Authors & Referees and the Editorial Policy Checklist.

Statistical parameters

When statistical analyses are reported, confirm that the following items are present in the relevant location (e.g. figure legend, table legend, main text, or Methods section).

n/a	Confirmed	
☐	☒	The exact sample size (*n*) for each experimental group/condition, given as a discrete number and unit of measurement
☐	☒	An indication of whether measurements were taken from distinct samples or whether the same sample was measured repeatedly
☐	☒	The statistical test(s) used AND whether they are one- or two-sided *Only common tests should be described solely by name; describe more complex techniques in the Methods section.*
☒	☐	A description of all covariates tested
☐	☒	A description of any assumptions or corrections, such as tests of normality and adjustment for multiple comparisons
☐	☒	A full description of the statistics including central tendency (e.g. means) or other basic estimates (e.g. regression coefficient) AND variation (e.g. standard deviation) or associated estimates of uncertainty (e.g. confidence intervals)
☐	☒	For null hypothesis testing, the test statistic (e.g. *F*, *t*, *r*) with confidence intervals, effect sizes, degrees of freedom and *P* value noted *Give P values as exact values whenever suitable.*
☒	☐	For Bayesian analysis, information on the choice of priors and Markov chain Monte Carlo settings
☒	☐	For hierarchical and complex designs, identification of the appropriate level for tests and full reporting of outcomes
☒	☐	Estimates of effect sizes (e.g. Cohen's *d*, Pearson's *r*), indicating how they were calculated
☐	☒	Clearly defined error bars *State explicitly what error bars represent (e.g. SD, SE, CI)*

Our web collection on statistics for biologists may be useful.

Software and code

Policy information about availability of computer code

Data collection	NIS Elements software. MotorMonitor Software (Kinder Scientific, Poway, CA). FreezeFrame (Actimetrics, Wilmette, IL). Video camera system (ViewPoint, Lyon, France). nVista HD (Inscopix, Palo Alto, CA). Custom code is available upon request.
Data analysis	GraphPad Prism v7. ImageJ 1.49v, NIH. Synaptic analysis was performed in Igor Pro using freely available routines (https://sites.google.com/site/tarotoolsregister/). FreezeView softwares (Actimetrics, Wilmette, IL). Inscopix Data Processing Software (v1.0.0.2273, Inscopix, Palo Alto, CA). MATLAB (Mathworks, Natick MA). Constrained Non-negative Matrix Factorization optimized for microEndoscopic data (CNMF-E) code from Zhou et al., Elife, 2018. CellReg code from Sheintuch et al., Cell Reports, 2017. Custom code is available upon request.

For manuscripts utilizing custom algorithms or software that are central to the research but not yet described in published literature, software must be made available to editors/reviewers upon request. We strongly encourage code deposition in a community repository (e.g. GitHub). See the Nature Research guidelines for submitting code & software for further information.

Data

Policy information about availability of data

All manuscripts must include a data availability statement. This statement should provide the following information, where applicable:

- Accession codes, unique identifiers, or web links for publicly available datasets
- A list of figures that have associated raw data
- A description of any restrictions on data availability

The data that support the findings of this study are available from the corresponding author upon request.

Field-specific reporting

Please select the best fit for your research. If you are not sure, read the appropriate sections before making your selection.

☒ Life sciences ☐ Behavioural & social sciences ☐ Ecological, evolutionary & environmental sciences

For a reference copy of the document with all sections, see nature.com/authors/policies/ReportingSummary-flat.pdf

Life sciences study design

All studies must disclose on these points even when the disclosure is negative.

Sample size	No statistical methods were used to pre-determine sample sizes but our sample sizes are similar to those reported in previous publications (see methods).
Data exclusions	At the end of each behavioral experiment (7 weeks following viral surgery), post-mortem control of viral and fiber optics placement was carried out to ensure appropriate targeting. 1 DIO-ChR2 injected mouse was discarded out of 7 animals (Fig. 5). This animal was used as a home cage control on perfusion day (day 21) for c-Fos analysis). Mice showing no obvious calcium transients were not included for behavioral analysis (approximately 50% of implanted mice). Calcium imaging traces without significant transients were excluded from analyses.
Replication	Several of our experiments were replicated using a complementary technique. Immunohistochemical analysis of c-Fos in DLS was reproduced twice in Supplementary Fig. 2a and Supplementary Fig. 2f-j. Rabies (Fig. 2a-b) and Canine (supplementary Fig. 4b) viral tracing as well as slice electrophysiological recordings (Fig. 2c-g) yielded similar results showing monosynaptic CA3 inputs onto DLS SST-INs. Characterization of SST-INs in DLS was reproduced twice by using immunohistochemical detection of SST (supplementary Fig. 5a) as well as by crossing SST-Cre mice with the reporter line Ai14 (supplementary Fig. 5b). Characterization of SST-INs projections to subcortical regions was reproduced twice by injecting an AAV-DIO-Chr2-eYFP into SST-Cre mice as well as Gad2-Cre mice (supplementary Fig. 5f). In vivo calcium imaging: These data were analyzed using two independent methods following a pre-processing step using Inscopix Data Processing Software (v1.0.0.2273, Inscopix, Palo Alto, CA) for motion correction. The pre-processed movies were then analyzed with (i) "constrained non-negative matrix factorization" (CNMF-E)"algorithm for ROI detection, fluorescence trace extraction followed by cell registration using CellReg (Fig. 3h-k). Alternatively, the videos were analyzed with principal component analysis and individual component analysis (PCA-ICA) algorithm (Inscopix Data Processing Software, v1.0.0.2273, Inscopix, Palo Alto, CA) for ROI detection, fluorescence trace extraction followed by cell registration (supplementary Fig. 6h-k). The control of DLS SST-INs on freezing behavior was replicated by using eNpHR3.0 to show an increase in freezing behavior (Fig. 4h) and ChR2 to demonstrate a decrease in freezing behavior (Fig. 5h).
Randomization	Age-matched, male mice (3-4 months old) were used for behavioral experiments. Cagemates were pseudo-randomly assigned to groups during virus injection (i.e., eYFP vs. ChR2).
Blinding	During testing, investigators were not blind to condition. However, results were replicated across several cohorts. Videos for behavioral scoring (i.e., freezing behavior) were analyzed using FreezeView softwares (Actimetrics, Wilmette, IL) during sessions without light application. For sessions in which mice received photostimulation (silencing), the light coming out of the implants prevented automatic scoring and was therefore independently scored by 2 investigators. Other analyses of behavior such as ambulation in the open-field was scored automatically using MotorMonitor Software (Kinder Scientific, Poway, CA). Anxiety assessment in the elevated plus maze and novelty suppressed feeding tests were carried out by 1 investigator blinded to treatment and/or genotype. Sahay (PI) selected individuals in the lab to perform independent scoring.

Reporting for specific materials, systems and methods

Materials & experimental systems

n/a	Involved in the study
☒	☐ Unique biological materials
☐	☒ Antibodies
☒	☐ Eukaryotic cell lines
☒	☐ Palaeontology
☐	☒ Animals and other organisms
☒	☐ Human research participants

Methods

n/a	Involved in the study
☒	☐ ChIP-seq
☒	☐ Flow cytometry
☒	☐ MRI-based neuroimaging

Antibodies

Antibodies used	Rabbit anti c-fos, Calbiochem PC38, 1:10,000 (Antibodyregistry.org: AB_2106755)(discontinued); different batches of rabbit, Santa Cruz SC52, 1:2,000-1:5,000 (Antibodyregistry.org: AB_2106783)(discontinued); rabbit anti-GFP, Life Technologies A11122, 1:500 (Antibodyregistry.org: AB_221569); chicken anti-GFP, Abcam AB13970, 1:2,000 (Antibodyregistry.org: AB_300798); mouse anti-CB, Swant 300, 1:5,000 (Antibodyregistry.org: AB_10000347); goat anti-SST, Santa Cruz SC7819, 1:400 (Antibodyregistry.org: AB_2302603); mouse anti-CR, Swant 6B3, 1:500 (Antibodyregistry.org: AB_10000320); mouse anti-PV, Millipore MAB1572, 1:2,000 (Antibodyregistry.org: AB_2174013); rabbit anti-NPY, Sigma N9528, 1:10,000 (Antibodyregistry.org: AB_260814); goat anti-Chat, Millipore AB144P, 1:400 (Antibodyregistry.org: AB_11214092); mouse anti-RGS14, UC Davis/ NIH NeuroMAB, 1:400 (Antibodyregistry.org: AB_10698026) . Donkey anti-rabbit, anti-mouse, anti-goat and/or anti-chicken Cy3, FITC or Cy5-coupled secondary antibody (Jackson ImmunoResearch, 1:500).
Validation	All antibodies are widely used and we defined the optimal antibody dilution by performing serial dilutions, including negative controls omitting the primary and secondary antibody. Immunohistological data were compared to in situ hybridization data freely available on the Allen Brain Atlas database and each antibody is referenced in the Antibodyregistry.org.

Animals and other organisms

Policy information about studies involving animals; ARRIVE guidelines recommended for reporting animal research

Laboratory animals	Male mice were housed four per cage in a 12 hr (7:00 a.m. to 7:00 p.m.) light/dark colony room at 22°C–24°C with ad libitum access to food and water. Age-matched, male mice (2-4 months old) were used for behavioral experiments. Cagemates were randomly assigned to groups during virus injection. Behavioral experiments took place between 8:00 a.m. and 6:00 p.m. All animals were handled and experiments were conducted in accordance with procedures approved by the Institutional Animal Care and Use Committee at the Massachusetts General Hospital and Boston University in accordance with NIH guidelines. 8 week-old C57BL/6J male mice were purchased from Jackson labs (Bar Harbor, ME). Rosa-CAG-LSL-tdTomato-WPRE::deltaNeo (Ai14) (C57BL/6J) mouse line harbors a loxP-flanked STOP cassette allowing transcription of CAG promoter-driven tdTomato following Cre-mediated recombination. Ai14 was purchased from Jackson labs (stock number 007914). Sst-IRES-Cre knock-in (C57BL/6J) mouse line expresses Cre recombinase in somatostatin-expressing neurons. SST-IRES-Cre was purchased from Jackson labs (stock number 028864). Gad2-IRES-Cre knock-in (C57BL/6J) mouse line expresses Cre recombinase in GAD2-expressing neurons. Gad2-IRES-Cre was purchased from Jackson labs (stock number 028867). Rosa-LSL-Tva-lacZ (mixed 129S6;C57BL/6J) mouse line has a loxed-STOP cassette allowing transcription of avian receptor Tva-lacZ fusion gene following Cre-mediated recombination. Rosa-LSL-TVA-lacZ mouse line was generously provided by Pr. Dieter Saur. Tail DNA from all offspring was genotyped by PCR to detect the presence of each transgene separately. All experiments were conducted with 8-16 week-old mice (unless indicated otherwise).
Wild animals	This study did not contain wild animals
Field-collected samples	This study did not contain field-collected samples